



HAL
open science

Properties of jet and surrounding material of GW/GRB 170817A

Houri Ziaeeepour

► **To cite this version:**

Houri Ziaeeepour. Properties of jet and surrounding material of GW/GRB 170817A. Monthly Notices of the Royal Astronomical Society, 2019, 490 (2), pp.2822-2837. 10.1093/mnras/stz2735 . hal-02017019

HAL Id: hal-02017019

<https://hal.science/hal-02017019>

Submitted on 5 Jul 2023

HAL is a multi-disciplinary open access archive for the deposit and dissemination of scientific research documents, whether they are published or not. The documents may come from teaching and research institutions in France or abroad, or from public or private research centers.

L'archive ouverte pluridisciplinaire **HAL**, est destinée au dépôt et à la diffusion de documents scientifiques de niveau recherche, publiés ou non, émanant des établissements d'enseignement et de recherche français ou étrangers, des laboratoires publics ou privés.

Properties of jet and surrounding material of GW/GRB 170817A

Houri Ziaeepour^{1,2}★

¹*Institut UTINAM, CNRS UMR 6213, Observatoire de Besançon, Université de Franche Comté, 41 bis ave. de l'Observatoire, BP 1615, F-25010 Besançon, France*

²*Mullard Space Science Laboratory, Holmbury St Mary, Dorking, Surrey RH5 6NT, UK*

Accepted 2019 September 23. Received 2019 September 23; in original form 2019 February 1

ABSTRACT

We use published data in radio, optical, and X-ray bands to analyse and model afterglows of GW/GRB 170817A. Our analysis is based on a phenomenological gamma-ray burst generator model, which we previously used to study the prompt gamma-ray emission of this important transient. We find a multicomponent model and a few of its variants that are consistent with broad-band ~ 1 yr observations of afterglows, once the contribution of kilonova in optical/IR band is taken into account. Considering beaming and off-axis view of relativistic outflows, we interpret the components of the model as approximately presenting the profile of a relativistic structured jet with a rapidly declining Lorentz factor from our line of sight, where it had a Lorentz factor of $\mathcal{O}(100)$, to outer boundaries, where it became a mildly relativistic cocoon with a relative velocity to light of ~ 0.4 – 0.97 . Properties of the ultra-relativistic core of the jet obtained here are consistent with conclusions from analysis of the prompt gamma-ray emission. In particular, our results show that after prompt internal shocks the remnant of the jet retained in some extent its internal collimation and coherence. Slow rise of the afterglows can be associated to low density of circumburst material and low column density of the jet. The long distance of external shocks from the merger, which could have been in part responsible for extensive thinning of the jet through expansion and energy dissipation before occurrence of external shocks, is responsible for the peak of emission being at $\gtrsim 110$ d after the merger. We discuss implications of these observations for origin and properties of circumburst material around binary neutron stars. This analysis confirms our previous results showing that an outflow with a Lorentz factor of ~ 2 – 5 cannot explain observed afterglows without an additional X-ray source or significant absorption of optical/IR photons.

Key words: gravitational waves.

1 INTRODUCTION

There is no general consensus about physics behind the unusual afterglows of the short GRB 170817A – the electromagnetic counterpart of the first detected Gravitational Wave (GW) from merger of a binary neutron star (BNS; LIGO Scientific Collaboration 2017a,b). This burst can be singled out by the faintness of its prompt gamma-ray and early X-ray afterglow, and its later brightening leading to the detection of an X-ray counterpart only after $\sim T + 10$ d (Evans et al. 2017; Margutti et al. 2017; Troja et al. 2017), where T is the trigger time of the Fermi-GBM (Dingus 1995) and Integral-SPI-ACS (Winkler et al. 2003) about 2 s after the chirp of the GW from the merger (Goldstein et al. 2017; Savchenko et al. 2017).

The initial interpretation of these observations was off-axis view of an otherwise ordinary short GRB (Alexander et al. 2017; Murguia-Berthier et al. 2017; Troja et al. 2017; Lazzati et al. 2018). Another popular explanation was emission from break out of a cocoon – a mildly relativistic ejecta with a Lorentz factor $\Gamma \sim 2$ – 3 (Kasliwal et al. 2017; Gottlieb et al. 2017; Hallinan et al. 2017; Nakar et al. 2018; Piro & Kollmeier 2017). However, the decline of flux in all three observed energy bands, i.e. radio (Mooley et al. 2017; Alexander et al. 2018; Dobie et al. 2018; Mooley et al. 2017, 2018b), optical (Lyman et al. 2018; Rossi et al. 2018; Lamb et al. 2019), and X-ray (D’Avanzo et al. 2018; Haggard et al. 2018; Hajela et al. 2018; Margutti et al. 2018; Nynka, Ruan & Haggard 2018; Troja et al. 2018a) after $\gtrsim T + 200$ d is much earlier than the prediction of a side viewed jet (Lazzati et al. 2016) (see also earlier versions of Lazzati et al. 2018). Predictions of jet break out (Gottlieb et al. 2017; Kasliwal et al. 2017) and cocoon (Mooley et al. 2017) models for 6 GHz band are compared with data taken up to $\sim T + 110$ d in Margutti et al. (2018) and are inconsistent

* E-mail: houriziaeepour@gmail.com

with observations. However, predictions of the break time are model dependent and some off-axis models such as those studied by Rossi et al. (2004) and Lamb & Kobayashi (2017) find a peak time $\sim \mathcal{O}(200)$ d, i.e. consistent with peak time of GRB 170817A afterglows. But, these works present general models and are not adjusted to special properties of GW/GRB 170817A.

Gradually it became clear that the presence of a highly relativistic component in the outflow at late times is inevitable. For instance, using relativistic hydrodynamic simulations of Duffell & MacFadyen (2013), and Duffell, Quataert & MacFadyen (2015) for determining characteristics of the BNS merger outflow and asymptotic formulation of external shocks and synchrotron emission by Sari et al. (1998) for fitting the afterglows, Margutti et al. (2018) and Xie, Zrake & MacFadyen (2018) found that an outflow with a narrow relativistic core having a Lorentz factor of ~ 100 and a sheath/side lob with a Lorentz factor of $\Gamma \sim 3-10$, where our line of sight passes through with an angle of $\sim 20^\circ$, can explain observations up to $\lesssim 140$ d. Following the detection of superluminal motion of the radio afterglow due to an oblique viewing angle, Mooley et al. (2018a), Ghirlanda et al. (2019) concluded $\Gamma \sim 4$ for the outflow at ~ 230 d and estimated an initial Lorentz factor of ~ 10 for the jet at the time of prompt gamma-ray. They also estimated an off-axis angle of $\theta_v \sim 20^\circ$ for the line of sight. In a later work Mooley et al. (2018b) ruled out the cocoon/jet break out model suggested by some of these authors in their previous works and fit the spectrum with a phenomenological non-linear two-component broken power-law expression (Beuermann et al. 1999) in contrast to a simple power-law used (e.g. in Mooley et al. 2017; Margutti et al. 2018; Troja et al. 2018b). Finally, using all the observations in radio, optical/IR, and X-ray during the first year after the merger event, Lamb et al. (2019) found that the data can be fit by a 2-component jet model consisting of an ultra-relativistic component with $\Gamma \gtrsim 100$ and a relativistic component with $\Gamma \sim 5$.

In Ziaeeppour (2019) we used a phenomenological shock and synchrotron emission model to show that an outflow with a Lorentz factor of $\sim 2-3$ underestimates X-ray flux. The same phenomenological formulation was used in Ziaeeppour (2018) to model the prompt gamma-ray emission of GW/GRB 170817A. The range of Lorentz factor studied in Ziaeeppour (2019) is the same as those employed in the early literature on this burst – especially those associating the unusual afterglows to a mildly relativistic cocoon.¹ The reason for this choice was the assumption that at $t > T + 10$ d, i.e. well after internal shocks, the weak ultra-relativistic jet responsible for the faint prompt gamma-ray burst had dissipated its energy and its Lorentz factor had to be much smaller than $\Gamma \sim 10-100$ concluded in Ziaeeppour (2018). In line with the same argument, the observed deficiency of X-ray with respect to optical and radio concluded from simulations with aforementioned low Lorentz factor implied either an additional source of X-ray – for instance a contribution from the decay of radioactive elements produced by the kilonova – or a significant absorption of optical photons.

In this work we use the same phenomenological model as the one employed in Ziaeeppour (2018, 2019), but we drop the assumption of a dissipated jet. We show that a multicomponent model, including both ultra-relativistic and mildly relativistic components, and a kilonova can explain all the data. The components of the model approximately present angular profiles of density and Lorentz factor of the polar ejecta from the BNS merger and its evolution. We use

this model and properties of circumburst material to investigate reasons behind the late brightening of the afterglows.

In Section 2 we describe the model and compare it with afterglow models of GW/GRB 170817A in the literature. Interpretation of the three-component model is discussed in Section 3. Parameters of the phenomenological model are summarized in Appendix A. Degeneracies of these parameters are discussed in details in Ziaeeppour & Gardner (2011), Ziaeeppour (2018) and are not repeated here. Nonetheless, to investigate whether conclusions made in Section 3 can be significantly impacted by them, in Appendix B we present light curves of several variants of our best model and discuss their properties. Our results are summarized in Section 4.

2 AFTERGLOW MODEL

The phenomenological model of relativistic shocks and synchrotron-self-Compton emission of Ziaeeppour (2009), Ziaeeppour & Gardner (2011) used in this work is reviewed in Ziaeeppour (2018, 2019) and we do not repeat it here. Nonetheless, for the sake of self-sufficiency definition of parameters of the model are given in Table A1. Moreover, some details about how kinematics of the shock and dynamics of the emissions are modelled and related are given in Section 3.3.2. They will be used for interpretation of GW/GRB 170817 models.

It is important to remind that there is a significant difference between our approach, in which a synthetic burst is generated for a set of input parameters characterizing the jet and its surrounding, and modelling of afterglows according to asymptotic power-law behaviour of light curves and spectra based on the original calculations of general aspects of synchrotron emission from external shocks by Sari et al. (1998). Notably, in our approach simulated bursts explicitly depend on distance and column density of the jet and thereby give an assessment of these quantities. Although analysis of GW/GRB 170817A afterglows (e.g. by Margutti et al. 2017, 2018; Alexander et al. 2018; Hotokezaka et al. 2018) are based on the jet characteristics obtained from Magneto-Hydro-Dynamics (MHD) or relativistic hydrodynamics simulations, synchrotron emission is calculated according to the asymptotic formulation of Sari et al. (1998), which estimates power-law behaviour of afterglows in a given energy band by comparing emission's frequency with characteristic and cooling frequencies of accelerated electrons. However, backreaction of shocks and energy dissipation are not explicitly taken into account. The model used here is also phenomenological and an approximation. In particular, some of the important processes and quantities, which cannot be easily formulated from first principles, are presented by parametrization and their initial values are chosen by hand. Nonetheless, the model takes into account in a systematic manner backreaction and evolution of physical properties important for the synchrotron/self-Compton emission. Moreover, the model is applicable to both internal (Ziaeeppour & Gardner 2011; Ziaeeppour 2018) and external shocks, and thereby allows to compare and to verify consistency of parameters obtained from the two types of emission in the same framework.

Due to the large number of parameters in the model and CPU time necessary for each simulation it is not possible to perform a systematic search for the best fit to data.² Nonetheless, despite their

¹In the literature ‘mildly relativistic’ indicates a large range of Lorentz factors from $\Gamma - 1 \sim \mathcal{O}(0.1)$ to $\Gamma \sim \mathcal{O}(1)$.

²To give an idea about calculation time, on a 3.06 GHz Intel Duo CPU T9900 processor a simulation with three time intervals – regimes – takes about 20–30 min without calculating inverse Compton and about two times longer with inverse Compton. If only five parameters are changed on a lattice

Table 1. Parameter set of simulated models.

Comp.	mod.	γ'_0	r_0 (cm)	$\frac{\Delta r_0}{r_0}$	$(\frac{r}{r_0})_{\max}$	p	γ_{cut}	κ	δ	ϵ_B	α_B	$\epsilon_e \gamma_e$	α_e	\dot{N} (cm^{-3})	n'_c (cm^{-2})
Ultra. rel. (C1)	1	130	10^{16}	10^{-7}	1.5	1.8	100	-0.5	0.5	0.08	-1	0.1	-1	0.04	5×10^{22}
	2	–	–	–	15	–	100	0.3	0.1	–	0	–	0	–	–
	2	–	–	–	20	–	100	0.4	0.05	–	1	–	1	–	–
Rel. (C2)	1	5	10^{16}	10^{-6}	2	2.1	100	-0.5	1	0.08	-1	0.1	-1	0.04	10^{23}
	2	–	–	–	40	–	100	0.4	0.1	–	0	–	0	–	–
	2	–	–	–	100	–	100	0.5	1	–	1	–	1	–	–
Mildly rel. (C3)	1	1.06	1.5×10^{16}	10^{-2}	1.5	1.8	100	-0.5	1	0.08	-1	0.02	-1	0.008	10^{24}
	2	–	–	–	10	–	100	0.	0.1	–	0	–	0	–	–
	2	–	–	–	10	–	100	1	1	–	1	–	1	–	–

Notes. *Each data line corresponds to one simulated regime, during which quantities listed here remain constant or evolve dynamically according to fixed rules. A full simulation of a burst usually includes multiple regimes (at least two).

*Horizontal black lines separate time intervals (regimes) of independent simulations identified by the label shown in the first column.

*A dash as value for a parameter presents one of the following cases: it is irrelevant for the model; it is evolved from its initial value according to an evolution equations described in Ziaeepour (2009), Ziaeepour & Gardner (2011); it is kept constant during all regimes.

apparent arbitrariness, physically acceptable values of parameters are not completely random. The distance of external shocks from central source is determined by wind nebula surrounding progenitor neutron stars and its termination shock. In pulsars wind nebula extends to $\sim 10^{15}$ – 10^{17} cm (Chatterjee & Cordes 2004; Slane 2017; Posselt et al. 2018). But its dependence on the properties of neutron stars and their evolution is not well understood. Our simulations show that an initial distance of $\sim 10^{16}$ cm, which is in the logarithmic middle of the range given here leads to acceptable fit to the GW/GRB 170817A data.

The density of circumburst material on which the jet/outflow is shocked has a lower limit of $\lesssim 0.04 \text{ cm}^{-3}$, corresponding to the interstellar medium (ISM) density in the host concluded from the absence of significant neutral hydrogen in NGC 4993 (Hallinan et al. 2017). The spectrum of accelerated electrons in the shock is also fairly constrained to ~ 2 by Particle In Cell (PIC) simulations (Spitkovsky 2008). We do not consider any external magnetic field in the simulations presented here. The remaining parameters define the geometry of ejecta and surrounding material, and are adjusted by trial and error to fit the data as good as possible.

We find that a three-component model consisting of a diluted ultra-relativistic jet with $\Gamma \sim \mathcal{O}(100)$, a relativistic outflow with $\Gamma \sim \mathcal{O}(10)$, and a mildly relativistic outflow/cocoon with $\Gamma - 1 \sim \mathcal{O}(0.1)$ can explain observations in radio and X-ray bands and satisfies upper limit constraint imposed on optical/IR data, see below for more details. From now on we call these components C1, C2, and C3, respectively. Parameters of the model for these components are listed in Table 1. We remind that as the parameter space was not systematically searched, values of parameters for the best model given here should be treated as order of magnitude estimations. For this reason we do not provide any uncertainty for them. To see how variation of parameters can affect light curves and spectrum, and whether there is large degeneracies in the parameter space, which may invalidate interpretation of the model and its comparison with data, in Appendix B we present light curves of several variant models for each of the above components and

with five nodes for each, the total calculation time without inverse Compton would be $\sim 10^5$ min or about 130 d. In practice more than five parameters should be adjusted to find the best models and the time necessary for a systematic search would be much longer than above estimation.

compare them with the model presented in Table 1. Notably, the model presented in Fig. B3(a) for component C3 has a Lorentz factor of 4, similar to estimations from apparent superluminal motion of radio counterpart (Mooley et al. 2018a). It fits radio data up to $\sim T + 200$ d roughly as good as C3 in Table 1. However, at later times the latter provides a better fit. See Section 3.2 for further discussion of these models.

2.1 Data used for comparison with models

For comparing models with observations we use published data from various sources:

Radio data are in 5–6 GHz radio band taken from D’Avanzo et al. (2018) except for the last two points which are taken from Dobie et al. (2018) and Mooley et al. (2018b). The radio data in D’Avanzo et al. (2018) is reproduced from observations of Hallinan et al. (2017) and Mooley et al. (2017).

Optical/IR observations are in r and i or energetically close bands/filters i.e. R , *HST F606W*, and *HST F814W*. For $< T + 10$ d the data are taken from Soares-Santos et al. (2017). The R magnitude at $\sim T + 10$ is taken from Pian et al. (2017), r magnitude at $\sim T + 110$ is from Lyman et al. (2018), *HST F606W* at $\sim T + 134$ from D’Avanzo et al. (2018) (originally from Margutti et al. 2018), *HST F814W* magnitude at $\sim T + 160$ from Rossi et al. (2018) and *HST F606W* magnitude at later times from Lamb et al. (2019). Magnitude m is changed to flux density F by using $F(\text{ph/sec/cm}^2) = 10^{-0.4(m + 48.6) + 23} (\Delta\lambda/\lambda) \times 1.509 \times 10^3$.

X-ray data are in 0.3–8 keV for Chandra observations and 0.3–10 keV for data taken by the Swift-XRT and by the *XMM-Newton*. For the epoch before $\sim T + 9$ d only two upper limit for X-ray flux is available: an upper limit for time interval $\lesssim T + 10$ d from the Neil Gehrels Swift-XRT (Evans et al. 2017) and an upper limit at $\sim T + 2.2$ from Chandra observatory (Troja et al. 2017). The X-ray counterpart was detected and followed up later and we use data from Chandra observations at $\sim T + 9$ d (Margutti et al. 2017), $\sim T + 16$ d (Troja et al. 2017), $\sim T + 110$ (Margutti et al. 2018), *XMM-Newton* observation at $\sim T + 134$ d (D’Avanzo et al. 2018), Chandra observations at $\sim T + 260$ d (Nynka et al. 2018; Troja et al. 2018a), and at $\sim T + 359$ d (Haggard et al. 2018).

We did not attempt to homogenize these heterogeneous data for not to add further uncertainties. This fact and mismatch between

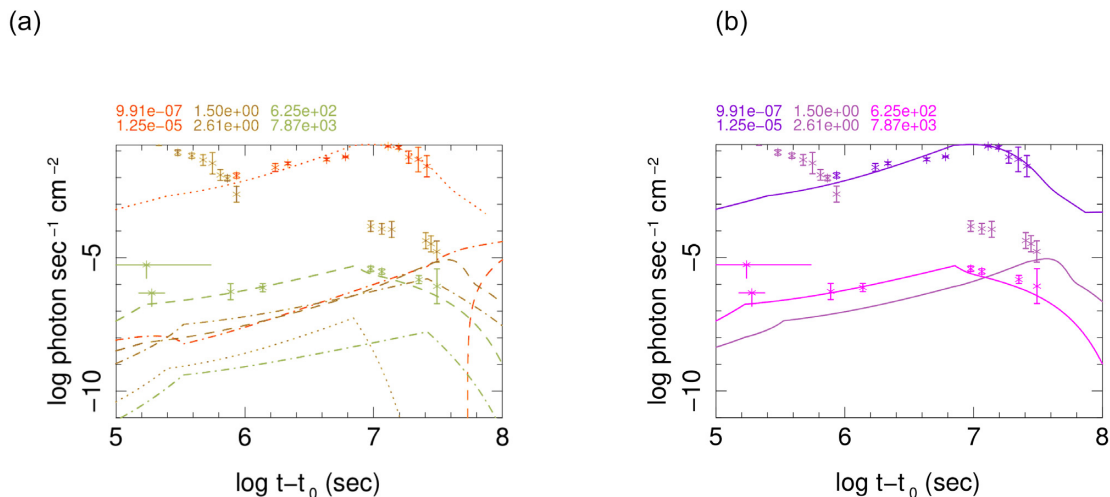


Figure 1. (a) Radio, optical/IR, and X-ray light curves of simulated three-component. Left-hand panel: Light curves of the three components: ultra-relativistic (C1) (dash lines), relativistic (C2) (dash-dot), mildly relativistic (C3) (dotted lines). The energy range for each band is written on the top of each plot in the same colour/grey scale as the curves. Stars and upper limits present the data described in Section 2.1. (b) Sum of the light curves of the three components: radio (magenta/light grey), optical (purple/medium grey), X-ray (dark purple/dark grey).

observations and simulated bands should be taken into account when models are compared with data.

After the detection of the prompt Gamma-ray spikes by the Fermi-GBM (Goldstein et al. 2017) and the Integral-IBIS (Savchenko et al. 2017) GW/GRB 170817 is not detected in high energy electromagnetic bands. Only an upper limit on any extended emission in 15–50 keV band is estimated from Swift Survey data by averaging background counts per 16 d from $\gtrsim T + 2$ s to $\sim T + 1$ yr (Krimm, Private Communication).

2.2 Comparison with observations

Fig. 1(a) shows light curves of each component of the model and Fig. 1(b) the total light curves in each band. We notice that X-ray and radio light curves have much better fit to data than simulated optical light curve. However, we know that optical data, especially at early times, is dominated by kilonova emission (Covino et al. 2017; Cowperthwaite et al. 2017; Nicholl et al. 2017; Smartt et al. 2017) and cannot be modelled with shock/synchrotron emission. Thus, presentation of early optical data in Fig. 1 and other light curve plots in this work is for the sake of completeness. Although a priori kilonova contribution can be modelled and removed, the residual would be model dependent. For this reason, we show optical data as it is observed and use it as an upper limit for the GRB contribution, which should be respected by any model of GRB 170817A afterglows. As the model presented in Fig. 1 (and some of its variants discussed in Appendix B) fit well radio and X-ray data, we presume that their prediction for optical emission should be reliable. Under this assumption, these models show that after $t_{kn} \sim T + 200$ to $\sim T + 300$ d – depending on the model – kilonova contribution in optical/IR emission was not anymore significant and the afterglow was dominated by synchrotron emission from external shocks of the relativistic outflow.³ This estimation for the time of kilonova fainting t_{kn} is consistent but somehow larger

than that by Waxman, Ofek & Kushnir (2019), who find $t_{kn} \gtrsim 100$ d. However, due to degeneracies in the parameter space of their kilonova emission model Waxman et al. (2019) do not fit it to data. Moreover, synchrotron light curves used for estimating GRB contribution are one possibility between many (see the discussion of degeneracies in Appendix B). Other works on the evolution of the kilonova emission (e.g. Kasen et al. 2017; Smartt et al. 2017; Metzger, Thompson & Quataert 2018; Kasen & Barnes 2019) are limited to initial tens of days after merger and cannot be compared with late optical data. Thus, we conclude that at present a satisfactory model for late optical emission of kilonova is not available.

Another assessment of the performance of the model can be made by comparing simulated spectrum with the photometric spectrum reconstructed from observations shown in Fig. 2(a). It shows good consistency between simulated spectrum and the data. As expected, amplitude of optical emission at $\sim T + \mathcal{O}(10)$ d is higher than the model. Moreover, due to the dominant contribution of kilonova emission the pseudo-spectrum of energy flux shown in Fig. 2(b) at this epoch is significantly different from those of later times. In this plot if we neglect optical data and use only radio and X-ray (dotted lines in Fig. 2b), spectra at all observation epochs have similar behaviour. Of course, a two-point pseudo-spectrum is a very crude presentation of the broad-band spectrum. Nonetheless, it is not affected by kilonova emission. Fig. 2(c) shows the evolution of spectral slope, which is similar to afterglows of other GRBs, namely softer during earliest observations around $T + \mathcal{O}(10)$ d, gradually becomes harder until the peak of emissions around $T + 110$ d, and finally softens at later times. The last data point in Fig. 2(c) is obtained from radio and X-ray data with largest uncertainties (see Fig. 1b) and apparent increase of slope and hardening of spectrum during last observation is very uncertain.

³Note that in addition to model dependence one has to take into account the heterogeneity of the optical/IR data and mismatch with the simulated energy band. For these reasons the time of dominance of synchrotron with

respect to kilonova contribution given in the text should be considered as nominal rather than exact.

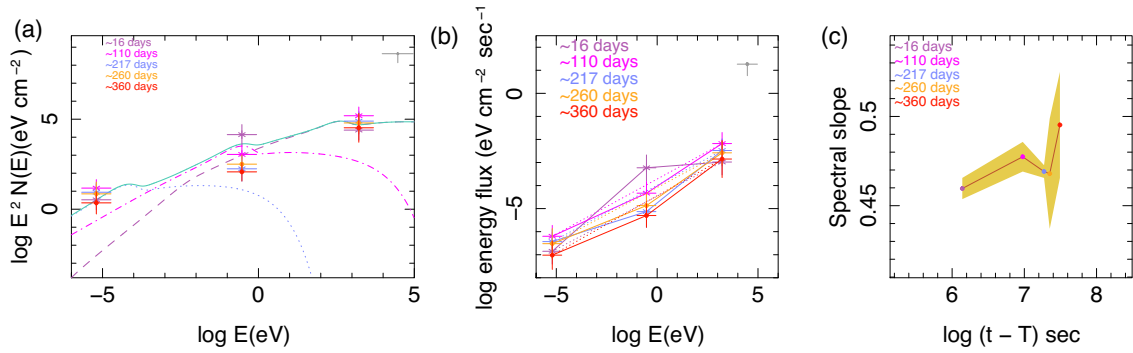


Figure 2. (a) Spectra of components and their sum: ultra-relativistic (C1) (dash line), relativistic (C2) (dash-dot), mildly relativistic (C3) (dotted line), sum of three components (full line). Crosses present observations at different times in radio, optical/IR, and X-ray, optical and radio bands. When data for a time interval were not available an interpolation has been used. The width of crosses presents the width of the corresponding filter and are much larger than observational uncertainties. The upper limit at $E \sim 15\text{--}50$ keV is from the Swift-BAT survey data (Krimm, Private Communication), see Section 2.1 for more details. To generate a pseudo-spectrum from flux measurements, we have normalized data such that X-ray at $T + 217$ d become equal to maximum of simulated spectrum in the simulated energy interval. (b) Spectrum of energy flux. The lines connecting the data points are added to facilitate the illustration of spectral variation. Similar to (a) plot width of crosses presents filler width. (c) Evolution of the slope of pseudo-spectrum using only radio and X-ray data, i.e slope of dotted lines in (b). The shaded region is uncertainty of calculated slopes.

2.3 Comparison with other analyses

As we described in the Introduction, some other authors have analysed late afterglows of GW/GRB 170817A by using multicomponent models including an ultra-relativistic jet. For instance, Alexander et al. (2018) and Margutti et al. (2018) consider a structured jet with a top-hat ultra-relativistic component with $\Gamma \sim 100$ in the inner $\theta \lesssim 9^\circ$, where θ is angle with respect to symmetry axis of outflow, and a relativistic flow which its Lorentz factor decreases in the angular interval $10^\circ \lesssim \theta \lesssim 60^\circ$ and has a mean $\Gamma \sim 10$. The authors consider a line of sight angle $\theta_v \sim 20^\circ$ from the jet axis. This model is very similar to the model described in the latest version of Lazzati et al. (2018). But Lorentz factor and energy profile of the jet in the two works are different. Lamb et al. (2019) consider two profiles for the jet, one similar to two-component model of Alexander et al. (2018) and Margutti et al. (2018). The other model assumes a jet with Gaussian energy and Lorentz factor profiles. Both models find a small central/core angle of $\lesssim 5^\circ$. In their two-component model high and low Lorentz factors are ~ 100 and ~ 5 , respectively. However, in the Gaussian model on-axis Lorentz factor can be as large as $\gtrsim 900$. Mooley et al. (2018b) model light curves of afterglows with a phenomenological function, which effectively has two coupled components. A priori they can be related to their Lorentz factor and density profiles. However, the complicated and non-linear form of this model make any physical interpretation difficult.

A question arises here: Is the presence of an ultra-relativistic component in our models and those cited in the previous paragraph inevitable? The existence of such a component means that our line of sight passed through the ultra-relativistic core of the jet. However, several authors find that the data can be fit with synchrotron emission of a jet with a Lorentz factor $\lesssim 10$ in our direction. For instance, Xie et al. (2018) find several variants of such models and show that they fit the data up to $\lesssim 150$ d. However, none of their models fit earliest X-ray data and aside from radio bands their data set include only a couple of points in X-ray and optical/IR. The model of Margutti et al. (2018) and Alexander et al. (2018) reviewed in the previous paragraph has an ultra-relativistic core with $\Gamma \sim 100$ up to $\theta \sim 9^\circ$,

but the viewing angle of $\lesssim 20^\circ$ found by these analyses means that the line of sight passes through a region with a Lorentz factor $\ll 100$ – they do not indicate the exact value of Lorentz factor on the line of sight. Similar to Xie et al. (2018) their model under estimates early X-ray data. To these examples one should add other models, namely cocoon (Mooley et al. 2018a,b; Nakar et al. 2018) and cocoon break out (Gottlieb et al. 2017; Kasliwal et al. 2017), which have much smaller Lorentz factors. None of these models is consistent with late X-ray data and overestimate its flux. Their consistency with optical data is also uncertain. Interestingly, with publication of later data, a general trend in the literature towards models with larger Lorentz factors is discernible – specially in works using observations up to ~ 200 d and beyond. For example, in earlier versions of Lazzati et al. (2018) a Lorentz factor of $\lesssim 10$ was associated to the jet. But in the final version of this work, which includes more data, the value of Lorentz factor is increased to $\mathcal{O}(100)$. Lamb et al. (2019) who use observations from earliest time to roughly 1 yr after merger find a Lorentz factor $\gtrsim \mathcal{O}(100)$. In conclusion, it is unlikely that the necessity of an ultra-relativistic Lorentz factor along our line of sight found here be due to degeneracies or quirk of our models.

In addition to differences in Lorentz factor on the line of sight, predictions for time of kilonova decay t_{kn} from modelling of GRB 170817A in the literature are not the same and are somehow shorter than $t_{kn} \sim 200\text{--}300$ d obtained from the model of Table 1 and its variants in Appendix B. Specifically, GRB afterglow models of (Troja et al. 2018c; Lamb et al. 2019; Wu & MacFadyen 2019) seem to fit optical data at $\gtrsim T + 100$ d. A priori this means that a $t_{kn} \lesssim 100$ d can be concluded from these works. However, they do not show early optical/IR data points and do not explicitly discuss the contribution of kilonova in the optical flux. In fact, it seems that they adjust the models to fit optical data after ~ 100 d. In this case, the time of kilonova decay in their models is a prior rather than a posterior conclusion derived from data. By contrast, as described earlier, in selection of plausible models here optical data were only considered as an upper limit and no attempt was made to fit simulated light curves in this band.

3 INTERPRETATION

3.1 Origin of ultra-relativistic component

In what concerns the Lorentz factor of the ultra-relativistic component of our model and similar models in the literature, they are consistent with analysis of Ziaeeepour (2018). Indeed, modelling of the prompt gamma-ray emission of GW/GRB 170817A shows that the best estimation for the Lorentz factor of the jet at the end of main gamma-ray spike is $\gtrsim 100$.

A priori it is not expected that a relativistic jet preserves its Lorentz factor during propagation from the site of internal shocks, which in the case of GW/GRB 170817A was at $r_i \equiv r_0 \sim \mathcal{O}(1) \times 10^{10}$ cm from merger (Ziaeeepour 2018), up to its collision with the ISM or circum-burst material at $r_e \equiv r_0 \sim \mathcal{O}(1) \times 10^{16}$ cm, in which afterglows are generated. Weaker late internal shocks, cooling of shocked material, and shocks on circum-merger material between r_i and r_e can dissipate kinetic energy of the jet and decelerate it. Indeed, weak gamma-ray and X-ray spikes and continuous emission are observed in both long (Willingale et al. 2006) and short bursts (Montanari et al. 2005; Norris, Gehrels & Scargle 2010) and are interpreted as emission from internal shocks of side lobes – high-latitude regions – of the jet (Takami et al. 2007) or weaker on-axis internal shocks (Willingale et al. 2006; Ziaeeepour & Gardner 2011).

Shocks on the material close to the BNS can be simulated by considering short distance external shocks similar to models presented in Figs B1(d)–(f), which have $r_e = r_0 = 10^{13}$ cm or $r_e = r_0 = 10^{15}$ cm. Because in these simulations the value of κ , which parametrizes variation of ISM/circum-burst material density with distance from centre, is the same as C1 (and its variants), their ISM/circum-burst material can be considered as extension of the same distribution as those at longer distances in C1. Thus, they present interaction of the ultra-relativistic jet with material near the merger. An important property of these simulation is that their emissions peak at early times and along with weak late internal shocks, they could a priori produce a plateau regime around $\lesssim T + 10^5$ s. Such behaviour has been observed in some short GRBs such as GRB 070724A, GRB170127B, and GRB 111020A. The latter GRB is an interesting case because it occurred at redshift 0.02 (Tunncliffe et al. 2014) and was only a few times brighter than GRB 170817A. Unfortunately, no early X-ray data are available for GRB 170817A and emission from circum-merger shocks cannot be investigated.⁴

Simulations presented in this work and those reviewed in Section 2.3 are the evidence that despite energy loss, a fraction of ultra-relativistic jet had survived without significant dissipation.⁵ Comparing the column density of the ultra-relativistic component C1 in Table 1 (and its variant in Fig. B1b) with the initial column density of the jet before internal shocks, which according to analysis of Ziaeeepour (2018) was 10^{25} cm⁻², shows that it is ~ 200 folds less than what it was pre-prompt emission. Assuming that dissipation of the second fainter and softer prompt spike corresponds to relativistic component C2 listed in Table 1 and its variants discussed in Section B2, we observe that its column density had become

~ 5 – 50 folds lower, i.e. reduced from 5×10^{23} cm⁻² to 10^{23} cm⁻² in C2 in Table 1 or to 10^{22} cm⁻² for models in which Lorentz factor $\gamma'_0 = \Gamma = 30$, i.e. the same as the second prompt gamma-ray peak. Evidently, there is no proof for any relation between C2 model and the second spike in the prompt gamma-ray because time resolution of late observations does not allow us to discriminate between afterglows of different density shells. Nonetheless, it is reasonable to presume that late time slower component include contribution from slower and more easily dissipatable part of the prompt outflow. Alternatively, rather than considering these models as competitive, they may be considered as finer decomposition of jet at late times, where the model with $\Gamma = 30$ presents a highly reduced remnant of second peak and C2 in Table 1 presents dissipated and laterally expanded remnant of both prompt shells. In this case, column densities and/or thickness of active regions of these components must be slightly smaller than what is given in Table 1 and Fig. B2 to make the total emission consistent with data, see Section B2 for more details. In any case, these variant models and their parameter space are consistent with our warning in Section 2 that values of parameters must be considered as order of magnitude estimations. Another important conclusion from variant models presented in Appendix B is that it does not seem possible to explain observed data with a one-component or even two-component model.⁶

If the jet were an adiabatically expanding cone, its column density had to decline by a factor of $\sim (r_i/r_e)^{-2} \sim 10^{12}$ where r_i and r_e are distance from centre when internal and external shocks occurred, respectively. The much smaller dilation factors we find for the three-component model means that the material inside the jet had preserved in some extent its internal coherence and collimation – most probably through imprinted electric and magnetic fields in the plasma – and its expansion was not completely adiabatic and free. Alternatively, accretion of material between r_i and r_e could a priori compensate reduction of column density due to an adiabatic expansion. Assuming a power-law variation of jet's column density by accretion per unit fly length, i.e. $dn'_c(r)/dr = (\alpha n'_a(r_0)/r_0)(r/r_0)^{\alpha-1}$ and neglecting loss of kinetic energy to radiation, from conservation of momentum we find: $n'_c(r) = n'_0(r/r_0)^{-2} + n'_a(r_0)[(r/r_0)^\alpha - 1]$ and $\beta(r) = n'_0\beta(r_0)/[n'_0 + n'_a(r_0)(r/r_0)^\alpha - 1]$. For $r/r_0 = 10^6$ and $n'_c(r)/n'_0 \sim 200$, $\beta(r) \sim 2 \times 10^{-10}\beta(r_0)$. This means that the jet would be practically stopped by accreted material. Therefore, small reduction of column density could not be due to accretion. On the other hand, much smaller column density of C1 with respect to the prompt jet demonstrates that energy dissipation by prompt internal shocks, accretion of material close to the merger, and/or internal interactions and loss of internal coherence had indeed occurred and led to lateral expansion, and thereby dilation of the jet's core and reduction of its Lorentz factor, especially in its outer boundaries. Therefore, our assumption about dissipation of the ultra-relativistic jet in Ziaeeepour (2019) was justified. Furthermore, thanks to long and extended follow up of this transient, for the first time we are clearly detecting the tiny remnant of the ultra-relativistic core of the jet in a short GRB and can distinguish its signature from slower part of the polar outflow of the BNS merger.

⁴If such data existed, amplitude of light curves in Figs B1(d) and (e) could be adjusted to fit the data.

⁵One of shortcomings of the phenomenological model of Ziaeeepour (2009) and Ziaeeepour & Gardner (2011) is that it is deterministic and cannot give a probability or distribution for dissipated and non-dissipated particles in the jet.

⁶The necessity of a multicomponent model is the clear evidence that the phenomenological formulation used here is too simplistic. Notably, it does not take into account anisotropic density and Lorentz factor of particles inside the jet. Asymptotic formulation of Sari et al. (1998) has also this problem.

3.2 Jet profile and viewing angle

Since the observation of unusually faint prompt gamma-ray of GRB 170817A, understanding the underlying physics has been the subject of significant debate. Specifically, the viewing angle of the ejecta had a central role in the proposed explanations.

Observation of gravitational waves led to an estimation for orbital inclination angle of $18^\circ \lesssim \theta_{\text{in}} \lesssim 27^\circ$ (Mandel 2018). Moreover, superluminal motion of radio afterglow with an apparent speed of $\beta_{\text{app}} = 4.1 \pm 0.5$ is observed by Mooley et al. (2018a) and Ghirlanda et al. (2019) and in combination with information from light curves and standard shock and synchrotron model and jet simulation Mooley et al. (2018a) estimated an off-axis angle of $\sim 20^\circ \pm 5^\circ$ for the line of sight. The above value of β_{app} constrains Lorentz factor of the source to $\Gamma \gtrsim 4$. In this case, C3 component in Table 1 is not consistent with the observed superluminal motion. Nonetheless, a variant of C3 with $\Gamma = 4$ and smaller ISM/circumburst density and active region thickness presented in Fig. B3(a) satisfies superluminal constraint. It fits radio data as good as C3 in Table 1 up to $\sim T + 230$ d which coincides with the second observation epoch of Mooley et al. (2018a). However, at later times the model with smaller Lorentz factor is a better fit to the data.

In order to select the most probable model for radio emitting component some other issues must be considered. Formulation of the phenomenological model developed in Ziaeeepour (2009) and Ziaeeepour & Gardner (2011) assumes $\Gamma \gg 1$. Therefore, uncertainty of C3 simulation with Γ close to 1 and its parameters should be larger than other components. Moreover, estimation of the error on β_{app} measurement might have been too optimistic. Fig. 2 (and fig. 1 of extended data) of Mooley et al. (2018a) shows both error ellipses and synthesized beam shape, and explicitly says that the source was not resolved. Giving the fact that the size of the image displacement was comparable to beam size, the size of 1-sigma uncertainty ellipse seems too small. In addition, lateral expansion of the cocoon between two observations used for determining β_{app} , which were separated by ~ 150 d might have changed the position of image centroid (Lind & Blandford 1985; Grano & Piran 2012). It is expected that due to scattering and energy dissipation in the core of the jet, the cocoon becomes slower, denser, and expands laterally (Nishikawa et al. 2016). Therefore, its effective off-axis angle with respect to the line of sight might have changed between two observations, leading to larger apparent displacements. Thus, although β_{app} was certainly non-zero, it could be much smaller than published value, and thereby consistent with a smaller Lorentz factor. An alternative possibility is to consider both C3 in Fig. B3(a) and C3 in Table 1. In this case the former presents the state of outflow at angles further than C2 and the latter its state at even larger angles. Considering the uncertainty of data and parameters, such a four-component model is consistent with radio data. In any case, most of our conclusions remain valid for both $\Gamma \sim 1.1$ and $\Gamma \sim 4$ for the component C3, and both three and four component models. For this reason we only consider three-component model and discuss differences in interpretations for low and high Lorentz factor C3 whenever necessary.

As a final evidence for plausibility of a mildly relativistic component with small Lorentz factor, we remind direct observation of a cocoon in the long GRB 171205A and its associated supernova SN2017uk (Izzo et al. 2017), which measures $\beta \sim 0.3$ corresponding to $\Gamma \sim 1.05$, i.e. similar to C3 component in Table 1.

Giving the fact that synchrotron emission is highly directional and emission from a relativistic source is beamed, off-axis view of the jet has significant consequences for observations. For instance,

assuming a uniform Lorentz factor across the emission surface, a far observer receives oblique radiation only from a cone with half angle $\theta \sim \arcsin(1/\Gamma)$ around the line of sight. Therefore, if the jet of GW/GRB 170817 was structured, radiation received by an off-axis observer would be from jet's slower wings rather than faster core, and thereby dominated by photons with lower energies because they had been produced by weaker and less boosted shocks in the jet's high latitude (boundary) region. Defining maximum visibility angle $\theta_{\text{max}} \equiv \arcsin(1/\Gamma)$, its value for components C1, C2, and C3 of the model listed in Table 1 are $\theta_{\text{max}_1} \sim 0.5^\circ$, $\theta_{\text{max}_2} \sim 11.5^\circ$, and $\theta_{\text{max}_3} \sim 65^\circ$ or 14.5° for C3 in Table 1 and its alternative in Fig. B3(a), respectively.

Fig. 1 shows that each of the components of the model dominates the total emission in one of the three energy bands with observational data, and higher the Lorentz factor of the component, higher is the energy of its dominant emission among the three components.⁷ Taking into account the observed inclination of the BNS orbit and superluminal motion of radio counterpart, we interpret the three-component model as a structured jet, in which each component approximately presents characteristics of the jet and its shocks on the surrounding material from our line of sight up to outer boundary of the outflow. The value of θ_{max} for the components of the model are consistent with this interpretation.⁸ Accordingly, their Lorentz factor presents azimuthal variation of velocity inside the polar outflow of the merger up to a $\cos \theta$ factor, that is $\Gamma_{\text{simul}, i} = \Gamma_i(\theta_i)\cos\theta_i$, where θ_i is angle between centroid of component i of the model and the line of sight. They are constrained by $\theta_{\text{max}_i} : \theta_i \lesssim \theta_{\text{max}_i}$. In addition, θ_{max_i} affects estimation of parameters. Specifically, for C1 its effect is negligible and for C2 is about 10 per cent. If we consider the model with $\Gamma = 4$ for C3, the effect of off-axis is again about 10 per cent. But for C3 model in Table 1 it can be as large as 42 per cent.

Fig. 3 shows a schematic presentation of the structured jet, components of the model, and their positions with respect to our line of sight and to symmetry axis of the outflow – assumed to have the highest Lorentz factor. Simulations of particle acceleration by transfer of Poynting to kinetic energy in the polar outflow of mergers show that the direction of maximum acceleration somehow deviates from the rotation and magnetic field axes (Komissarov et al. 2009). Thus, using the estimation of orbit inclination, the angle between

⁷For the time being, the simulation code used in this work uses an analytical expression for determining synchrotron/self-Compton flux. Moreover, terms depending on higher order of θ , angle between emitting element and line of sight, are neglected. This is a good approximation when $\Gamma \gg 1$. Under this approximation θ dependence is only through a $(\cos(\theta) + \beta) \leq (\cos(\theta) + 1)$ factor, which must be integrated between $\theta_0 \geq -\theta_{\text{max}}$ and $\theta_1 \leq \theta_{\text{max}}$. However, angular size of emitting surface may be smaller than $2\theta_{\text{max}}$. In this case integration over maximum visible angle overestimate the flux. But the difference would be at most a factor of few and comparable to other uncertainties of the model. Indeed, for this and other simplifications and approximations applied to the model that we should consider parameters as order of magnitude estimations.

⁸Although formulation of relativistic shocks and synchrotron emission in Ziaeeepour (2009) and Ziaeeepour & Gardner (2011) is more systematic than standard approach, it remains very much simplified and phenomenological. For instance, it considers a uniform column density and Lorentz factor for the jet. However, GRMHD simulations show that these assumptions are not true and column density is a function of both Lorentz factor and angle. It is why three components are necessary to explain the data. Therefore, this division and characteristics of components must be considered as an effective and simplified description.

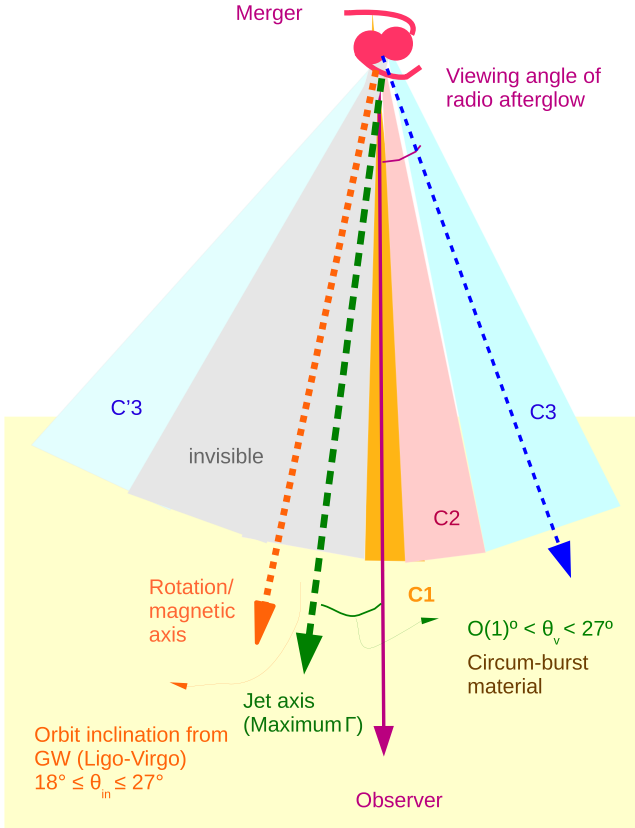


Figure 3. Schematic description of polar outflow of merger at the time of its encounter with circum-burst material. C1, C2, C3 refer to components of the simulated model. The grey shaded region on the opposite side of the jet with respect to observer’s line of sight is approximately invisible because of its large Lorentz factor and off-axis angle. Nonetheless, C’3 region which has even larger off-axis may be visible if its Lorentz factor is sufficiently low. Therefore, there can be a contribution to component C3 of the model from emission of this region. In any case, due to its large off-axis contribution of C’3 would be subdominant. For the sake of simplicity here we have assumed that magnetic field direction and rotation axis coincide. This may not be true.

our line of sight and direction of maximum Lorentz factor θ_v can be constrained as $\mathcal{O}(1)^\circ \lesssim \theta_v \lesssim 27^\circ$, independent of jet model. This interval is also consistent with estimations of viewing angle by Alexander et al. (2018), Margutti et al. (2018), and Mooley et al. (2018a).⁹

The knowledge of orbital inclination is not enough to constrain Lorentz factor profile up to its invisible core of the jet. Nonetheless, the sharp reduction of Lorentz factor from C1 which must be approximately along the line sight to C3 at $\lesssim 65^\circ$ or $\lesssim 14^\circ$ – depending on which C3 model is used – means that the visible part of the jet has an exponential $\Gamma \sim \Gamma_{\max} \exp(-(\theta + \theta_v)/\theta_\tau)$ or Gaussian $\Gamma \sim \Gamma_{\max} \exp(-(\theta + \theta_v)^2/2\sigma_\theta^2)$ profile, where θ is off-

⁹In Fig. 3 jet axis and the line of sight are assumed to be in the same projected side with respect to the rotation axis. Thus $\theta_v < \theta_{\text{in}}$. More generally, considering a cone around the line of sight with rotation axis on its surface, any line passing inside of its cross-section will have a smaller angle with line of sight than the rotation axis. Therefore, for $\theta_v > \theta_{\text{in}}$ the jet axis must be outside the cone. In this case the line of sight would be even further from jet axis than what is depicted in Fig. 3, and closer to non-relativistic or mildly relativistic cocoon. But, as discussed in the Introduction, such setup is not able to explain observations.

axis with respect to the line of sight, and θ_v is the angle between jet’s symmetry axis and line of sight. In absence of any knowledge about centroid of components, we must find the range of parameters which satisfy constraints on θ_i , and on parameters of the profile, namely $\theta_v > 0$, $\sigma_\theta^2 > 0$, and $\theta_\tau > 0$, respectively for Gaussian and exponential profiles.

Fig. 4 shows the consistency region for a Gaussian profile for both the model of Table 1 and its C3 variant shown in Fig. B3(a). Assuming $\theta_1 \sim 0.25^\circ$, for the model in Table 1 we find: $\theta_2 \sim 9^\circ - 11^\circ$, $\theta_3 \sim 12^\circ - 15^\circ$ for $\Gamma_{\max} < 1000$. Interestingly, this figure shows that the allowed values for viewing angle θ_v are strongly correlated with Γ_{\max} and are restricted to $5^\circ \lesssim \theta_v \lesssim 7^\circ$ for $\Gamma_{\max} \sim 250$ and $14^\circ \lesssim \theta_v \lesssim 18^\circ$ for $\Gamma_{\max} \sim 1000$. For second model the range of allowed angles are even more restricted: $\theta_v \sim 7.5^\circ - 8^\circ$, for $\Gamma_{\max} \sim 250$ and $\theta_v \sim 8^\circ - 15^\circ$, for $\Gamma_{\max} \sim 1000$, $\theta_2 \sim 10.5^\circ$, $\theta_3 \sim 11.5^\circ$, for $\Gamma_{\max} < 1000$. Considering the estimation of orbit inclination, the range of values for viewing angle obtained here confirms simulations of particle accelerations (Komissarov et al. 2009) that show a deviation between magnetic field – assumed to be the same as rotation axis – and maximum of acceleration. In the case of GW/GRB 170817A the deviation was $\sim [7^\circ - 15^\circ]$.

It is straightforward to see that in the case of exponential distribution θ_v and Γ_{\max} are fully degenerate. This degeneracy induces a relation between Lorentz factor and centroid of three components of the model, i.e. $(\theta_2 - \theta_1)/(\theta_3 - \theta_2) = \ln(\Gamma_1/\Gamma_2)/\ln(\Gamma_2/\Gamma_3)$. Using this relation and imposing $\Gamma_{\max} \sim 500$ and $\theta_1 = [0.25^\circ - 0.5^\circ]$, we find $\theta_v = [0.06^\circ - 0.3^\circ]$, $\theta_2 = [0.75^\circ - 1.5^\circ]$, $\theta_3 = [20.7^\circ - 41.4^\circ]$, $\theta_\tau = [0.06^\circ - 0.3^\circ]$ for the model in Table 1. For the alternative model θ_2 is the same, $\theta_v \sim 0.06^\circ$, $\theta_3 = [0.87^\circ - 1.74^\circ]$, $\theta_\tau = [0.08^\circ - 0.4^\circ]$. Small off-axis angles found for this profile are inconsistent with observed superluminal motion. Even for $\Gamma_{\max} \sim 1000$ off-axis angles remain too small to be consistent with a superluminal motion. Therefore, exponential profile is ruled out unless if superluminal β_{app} were much smaller than the value estimated by Mooley et al. (2018a).

The three-component model also provides information about density profile of the jet. Indeed, in agreement with simulations of jet acceleration to ultra-relativistic velocities (Komissarov et al. 2009), the density in the core of the accelerated jet, where Lorentz factor is maximum, is much lower than its surrounding. Moreover, as described earlier, at the time of external shocks the jet had been already subjected to partial dissipation. Thus, a large fraction of its content was scattered, slowed down, and acquired significant transverse momentum. These processes should make side lobes – *the cocoon* – slower and denser, and increase gradient of variation in the outflow. These expectations are consistent with the model presented here. In addition, fraction of kinetic energy of the jet transferred to electric and magnetic fields during shocks in outer boundary of the outflow are expected to be smaller. C3 component which is only mildly relativistic satisfies these expectations. However, Table 1 shows that the distance of this component from the centre at the onset of external shocks was ~ 50 per cent larger than the other components. This may have multiple origins: uncertainties of simulations when $\Gamma \gtrsim 1$ and/or delay in the formation of shocks due to small velocity of C3 and low density of ISM/circum-burst material.

3.3 Delayed brightening

A significant difference between the afterglow of GW/GRB 170817A and other short bursts is its seemingly intrinsic faintness at early times, i.e. at $\gtrsim T + 10^5$ s, when X-ray and optical follow up began, and its brightening at later times. However, none of

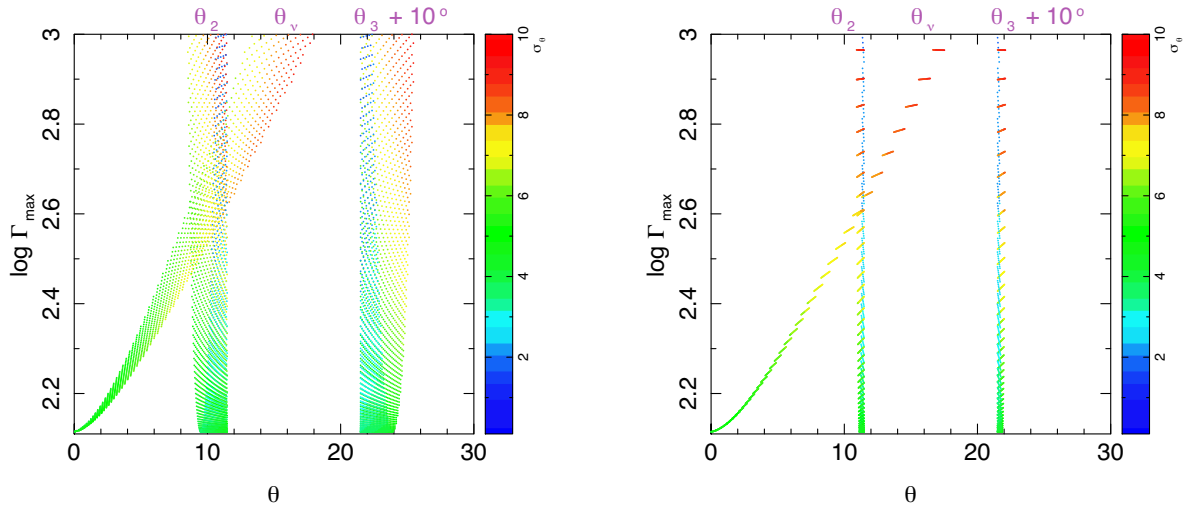


Figure 4. Parameter space of Gaussian profiles satisfying $\theta_v > 0$, $\sigma_\theta^2 > 0$, and having Lorentz factors obtained from simulations at centroid of each component. Left-hand panel: Model of Table 1; Right-hand panel: Model of Fig. B3(a). To make these plots $\theta_1 = 0.25^\circ$ is assumed and centroid angles of C2 and C3, i.e. θ_2 and θ_3 are selected in the range $\theta_{\max_1} \leq \theta_2 \leq \theta_{\max_2}$ and $\theta_{\max_2} \leq \theta_3 \leq \theta_{\max_3}$ and a solution for θ_v , Γ_{\max} , and σ_θ is obtained and added to $\theta_v - \log \Gamma_{\max}$ plane only if the solution satisfies above constraints (parabolic-like region). Approximately orthogonal regions correspond to $\theta_2 - \log \Gamma_{\max}$ (closer to origin) and $\theta_3 - \log \Gamma_{\max}$. The latter is shifted horizontally by 10° for clarity. The colour code presents σ_θ . Horizontal axis is a general θ variable and labels on the top axis show angle to which each track corresponds.

these conclusions are certain. Of course, as we showed in Ziaeeepour (2018), prompt emission of this burst was intrinsically the faintest among all GRBs with known redshift. Therefore, its early afterglow had to be equally faint. Indeed, X-ray flux upper limits of $\sim 10^{-13} \text{ erg s}^{-1} \text{ cm}^{-2}$ from observations of the Swift-XRT at $\gtrsim T + 1.6 \text{ d}$ in 0.3–10 keV (Evans et al. 2017) and $\sim 10^{-14} \text{ erg s}^{-1} \text{ cm}^{-2}$ in 0.3–8 keV from Chandra observations at $\sim T + 2.2 \text{ d}$ (Troja et al. 2017) are intrinsically the most stringent among short bursts with measured redshift (Fong et al. 2018). However, early X-ray afterglow of both short and long GRBs have variety of slopes (Kann 2012; Fong et al. 2015), see also simulations in Appendix B. Therefore, in absence of early observations, GW/GRB 170817A cannot be classified as an early dark burst.

Late brightening of the afterglow of this burst is not unique either. For instance, a slight brightening may have been observed at $\sim T + 10 \text{ d}$ for GRB 130603B and its accompanying kilonova (Fong et al. 2013). However, the excess found by Fong et al. (2013) was with respect to the model fitted to the data rather than in the observed flux. In any case, no other GRB has ever followed up for as long as GW/GRB 170817A. Therefore, we do not know how uncommon is the brightening of afterglows up to $\gtrsim T + 200 \text{ d}$. Afterglows of GRBs up to few thousands of seconds are most probably a superposition of weak internal shocks in what remains from the relativistic jet after the main prompt shock, and emission from external shocks (Willingale et al. 2006). Because a highly relativistic jet follows closely the prompt photons, the delay between their arrival to external material in general would be short – of order of few tens of seconds or less for ultra-relativistic jets and typical distances to circum-burst material. Assuming a narrow prompt spike, the delay between the prompt and onset of afterglow emission is $\Delta t \sim r_c/2c\Gamma^2$, where c is speed of light. For the model of Table 1 this delay is $\sim 4 \text{ s}$. For alternative models discussed in Appendix B with shorter distances to central object it is even shorter. Therefore, the early afterglows, if they were observed, were superimposed on a decaying *tail* emission from internal shocks,

and thereby time evolution of total emission depended on relative strength of decaying prompt tail and ascending afterglow. The absence of early brightening of afterglows in most GRBs means that they are dominated by *tail* emission of internal shocks. There are however exceptions. For instance, in long GRB 110213A (D’Elia et al. 2011) rapid decay of the prompt X-ray made ascending and peak of X-ray afterglow visible. But such cases are rare. More frequent case, specially in short GRBs, is the presence of a plateau. Best examples are GRB 070724A (Ziaeeepour et al. 2007) and GRB 070809 (Marshall et al. 2007), which have an early X-ray light curve with plateau similar to long GRBs.

Our simulations show that in the case of GW/GRB170817A the slow rise of the afterglow is due to low density of ISM/circum-burst material and low column density of the jet. The weakness of the jet was in part due to intrinsically low density and low Lorentz factor of polar ejecta – at least in our direction – and in part the result of the large distance of surrounding material from centre, that is $\sim 1000 \text{ AU}$ (see Table 1) rather than e.g. $\sim 100 \text{ AU}$ for the termination shock in the Solar system or $\sim 200 \text{ AU}$ for the recently detected NIR emitting material around the isolated neutron star RXJ0806.4-4123 (Posselt et al. 2018).

The initial suggestions about off-axis view and brightening of afterglows when the jet become dissipated and its content scattered to our line of sight, is not consistent with relatively early break of light curves in all three energy bands after $\sim T + 110 \text{ d}$. In fact, high Lorentz factor of X-ray emitting component found here and in the literature means that it is emitted very close to our line of sight. Therefore, the effect of distance and densities may be stronger than off-axis. It is however cautious to consider that this conclusion may be somehow biased and correlated to spatial resolution of our simulations, because as Table A1 shows, the initial/final width of synchrotron emitting region is defined as a fraction of initial distance of the shock from central source. Nonetheless, estimation of shock distance for this GRB in the literature and for other GRBs with various methods, such as cooling of thermal emission (Olivares et al. 2012) show that the range of distances obtained from simulation of

GRBs (Ziaeeepour & Gardner 2011) with the code used here are realistic.

3.3.1 Comparison with standard afterglow model

There is no essential difference between model of Ziaeeepour (2009), Ziaeeepour & Gardner (2011), and Blandford-McKee approach used by Sari et al. (1998). In both cases the shock is assumed to be radiative, i.e. falling material to the shock front (in its rest-frame) loses its kinetic energy as synchrotron radiation and makes the jet heavier. The only difference is that (Ziaeeepour 2009) formulation takes into account the back-reaction of this process in a systematic way and also allows evolution of induced fields, which cannot be formulated from first principles, in a parametric manner.

We remind that asymptotic behaviour of external shock emission formulated in Sari et al. (1998), which is used in works reviews in Section 2.3, considers a uniform spherical ejecta. Therefore, conclusions about viewing angle of the jet is based on the value of Lorentz factor and beaming of emissions from a relativistic source (Rybicki & Lightman 2004):

$$\frac{dP_e/d\Omega}{dP_r/d\Omega} = \frac{1}{\Gamma^2(1 + \beta \cos(\theta))}, \quad (1)$$

where P_e and P_r are emitted and received power in the observer frame, and θ is the angle between the line of light and the boost direction.

Comparing simulated spectrum shown in Fig. 2(a), which is up to uncertainties fully consistent with observations shown in the same plots, with figs 1(a) and (b) of Sari et al. (1998),¹⁰ we find that the total spectrum is consistent with a *fast cooling* model with $\nu_c < \nu_m \sim \nu_x$. However, as power of electrons Lorentz factor distribution $p \sim 2$ in all the components models of the model, the spectrum can also be classified as *slow cooling* with $\nu_m < \nu_c \sim \nu_x$. Spectra in Fig. 2(a) show that for each component the dominant emission band is very close to the peak of its spectrum – thus consistent with being dominant – and satisfies relations similar to those of the total spectrum given above. In particular, similarity of components spectra and their sum demonstrates why many of analysis in the literature reviewed in Section 2.3, specially those modelling GRB 170817A with a single relativistic component, find that mission in radio, optical/IR, and X-ray bands belong to a same power-law spectrum with a negative slope.

Synchrotron cooling frequency ν_c depends on the induced magnetic field, which in turn depends on the density of ISM; larger the density of accumulated (fallen) material, larger magnetic field and higher synchrotron characteristic frequency. It can be shown, using equations (4) and (6) of Sari et al. (1998), that $\nu_c \propto n^{-1} t^{-3/2}$, where n is density of accelerated charges. Therefore, for a given ν_c lower density means slower emission variation and longer duration of emission because of smaller induced magnetic field. However, in Sari et al. (1998) formulation the effect of jet column density is not explicit. We remind that the formation of a shock needs a significant density difference in the opposite sides of a boundary. Therefore, column density and density of ISM/circumburst material must be considered together. Slow evolution of emissions needs relatively low ISM/circumburst material and/or low density jet. The length of the jet/ejecta is also important. For the same column density, a longer jet is more diluted and its collision with circumburst

material generates less turbulence and less energy is transferred to induced fields. Moreover, if densities of colliding shells are low, the faster shell must sweep a longer distance inside the slow shell to accumulate material and form a shock front. In model C1 in Table 1 ISM/circumburst material density is in the middle of the range estimated for short bursts (Fong et al. 2015). However, column density of jet is low. In the variant model in Fig. B1(b), which is also a good fit to data, ISM/circumburst material density is lower, but a longer active region is assumed. Thus, for the ultra-relativistic component C1, the low density of colliding material may be the reason for long distance of external shocks from central source. By contrast, other components, which had larger column densities, have been radially more extended.

The total spectrum of the model in Fig. 2(a) does not show how $\sim \nu_c$ and ν_m change with time. Nonetheless, evolution of spectrum discussed in Section 2 show that, as expected, after the peak of emission $\sim \nu_c$ and ν_m of each component become smaller than what was their values before the peak.

In summary, we conclude that the early X-ray afterglow of GW/GRB 170817A at $\lesssim T + 10^5$ s had to be faint and dominated by weak internal shocks, and had declined quickly. A consequence of this conclusion, which unfortunately due to the lack of data cannot be verified, is that the claimed excess of UV emission at $\sim T + 1.6$ d (Covino et al. 2017; Cowperthwaite et al. 2017; Smartt et al. 2017) was indeed from kilonova rather than the afterglow of GRB 170817A. The origin of excess may be heating of a strong wind by neutrinos and strong magnetic field of the short-lived HMNS (Metzger et al. 2018)

3.3.2 Slope of afterglow rise

We notice that after initial fast rise the slope of light curves shown in Figs 1, B1, B2, B3 in the region far from the peak is $\sim 1 \pm 0.3$ and does not vary strongly.¹¹ To understand this behaviour we first remind that the asymptotic formulation of standard afterglow model by Sari et al. (1998) predicts a constant rising slope of ~ 0.5 for energy bands close but on the low energy wing with respect to the spectral peak. As we discussed in Section 3.3.1, in the multicomponent models of Table 1 and Appendix B the dominant emission band is close to the spectral peak. Therefore, having a roughly similar rising slope in these models is consistent with the asymptotic afterglow model. However, the latter underestimate the slope.

One reason for difference between predictions of the two models can be the fact that Sari et al. (1998) formulation depends only on the density of accelerated particles in the jet, which generate the shocked induced electromagnetic fields. The density of circumburst material \dot{N} on which the jet is shocked does not explicitly appear in the formulation. To see the importance of \dot{N} we notice that in the C1 alternative model of Fig. B1(a), in which only \dot{N} is less than that of C1 in Table 1, the rise slope of the X-ray light curve is ~ 0.7 and the peak flux is smaller. As explained in Section 3.3.1, time/radius dependence of quantities which determine strength of the shock, such as ISM/circumburst density and fraction of kinetic energy transferred to electrons and to induced magnetic field – parametrized by κ , α_e , and α_B , respectively – influence the slope of emission rise and the observed differences with the standard model. However, they are not the only parameters which influence the rise of emission. For instance, in the main C1 model the slope after

¹⁰We remind that spectra shown in Fig. 2 includes an additional energy factor with respect to those in figs 1(a) and (b) of Sari et al. (1998).

¹¹We thank the anonymous referee for bringing this point to our attention.

initial fast rise is ~ 1 . But it increases gradually up to the peak of the X-ray light curve.

A quantitative explanation of the rise slope in the framework of the model of Ziaeepour (2009) and Ziaeepour & Gardner (2011) needs an analytical solution of the model, which due to its complexity is not available. Nonetheless, we can use some of analytical results obtained in Ziaeepour (2009) and Ziaeepour & Gardner (2011) to understand which physical properties are involved in the rise of light curves and its dependence on the parameters of the model.

The phenomenological model of Ziaeepour (2009) and Ziaeepour & Gardner (2011) divides the process of relativistic shocks and synchrotron/self-Compton to two parts: (1) kinematic of the ejecta; (2) synchrotron/self-Compton emission. It calculates the evolution of kinematic by taking into account the total energy dissipated as synchrotron/self-Compton and obtain perturbative solutions for Lorentz factor $\Gamma(r)$ and column density $n_c(r) = n(r)\Delta r$, where r is an average distance of a narrow relativistic ejecta from centre and Δr is the width of shocked region – *the active region*. Under this approximation time t and r are not independent and $r(t) - r(t_0) = c \int_{t_0}^t \beta(t') dt'$. The results of this step is used to calculate synchrotron/self-Compton emission, from well-known textbook formulation of these processes, with the difference that it takes into account variation of electron and baryon densities in the jet/fast shell, their varying Lorentz factor, and possible radial density inhomogeneities of the slow shell/ISM. Time/radius dependence of these quantities connect kinematical and dynamical parts of the model. Additionally, in the case of internal shocks a total boost of colliding shells must be taken into account. However, this phenomenological formulation is unable to determine how the width of active region Δr changes with time/radius. Nonetheless, considering formation and decay of a shock front, the initial width of active region must be zero. It should grow gradually to a maximum and decline to zero at the end of the shock. A series of phenomenological models presenting such evolution is defined in Appendix A.

Under these approximations the synchrotron energy flux can be written as:

$$dP/(\omega d\omega) \propto r^2 \Delta r / \Gamma(r) \int_{\gamma_m}^{\infty} d\gamma_e n'_e(\gamma_e) f(\gamma_e, r), \quad (2)$$

where n'_e is the density of electrons and f is a function of r and electrons Lorentz factor γ_e , see e.g. equation (62) in Ziaeepour (2009) for full expression. The r^2 factor changes densities to total emission from volume of the active region. It reflects the fact that for the same density, column density, and jet opening angle, the total amount of emitting material is larger if the average radius of the shell is larger. Therefore, in addition to quantities related to microphysics of the ejecta and environment, geometrical setup, namely the initial distance of external shocks r_0 , extension of the ejecta and evolution of the thickness of active region Δr are crucial for rising and peak amplitude of emissions, see equation 30 and Appendix A in Ziaeepour (2009) for technical details. In particular, for the same densities and other parameters, longer distance to centre leads to longer rise time and higher and later peak emission.

The term $n'_e \Delta r$ in (2) can be considered as column density of electrons with Lorentz factor γ_e . Normalization factor of the distribution of electrons Lorentz factor is proportional to density of active regions $n' = n'_e / \Delta r$ and inversely proportional to minimum Lorentz factor of electrons $\gamma_m \propto \epsilon_e \propto (r/r_0)^{\alpha_e}$. However, due to non-linear term $f(\gamma_e, r)$ factors of Δr in (2) do not cancel each other. Evolution of $\Gamma(r)$ is also dependent on the phenomenological

exponent of δ , α_e , α_B , and κ , see equation (19) in Ziaeepour & Gardner (2011). As the values of these indices are the same in all the models discussed here – except the model shown in Fig. B1(e) in which $\kappa = 0$ – it is not a surprise that light curves have roughly the same rise slope. Nonetheless, due to the non-linearity of evolution equations the slope is not exactly the same in all the models. In addition, as mentioned earlier, it changes with time. This fact reflects the influence of complicated dynamics, which cannot be estimated by a simple asymptotic power law. For instance, the model in Fig. B1(e) (dotted line) has a faster rise than C1 in Table 1 because $\kappa = 0$, meaning that the density of circumburst material in this model does not decline at large distances from the merger. By contrast, in the model of Fig. B1(a), which has the same κ as C1, the rise of flux is slower because the density of circumburst material is much smaller than in C1. This shows how initial conditions and constant quantities in the model influence the dynamics of the emission.

3.4 Material surrounding the BNS

In the phenomenological model of Ziaeepour (2009) and Ziaeepour & Gardner (2011) the density of circumburst material and its variation with distance are defined by parameters n' and κ , respectively. Table 1 shows that $\kappa \neq 0$ and n' is not the same for all components of the model. This is probably an evidence that circumburst material was not only the ISM, which a priori should be independent of the merger and approximately uniform. Thus, additional material should have been present.

The origin of circumburst material and its properties can be traced back to the evolution of progenitor neutron stars. In young neutron stars and pulsars the distance to wind Termination Shock (TS) is $R_{TS} = \sqrt{\dot{E}/(4\pi\eta P)}$ where \dot{E} is the change in the rotational kinetic energy and P is average pressure in the wind nebula surrounding the neutron star (Slane 2017). After initial expansion of nebula and establishment of an approximately steady-state condition, the pressure inside the nebula is balanced with the ISM pressure and extension of pulsar nebula is stabilized to $R_{TS} \sim \mathcal{O}(0.1)$ pc (Slane 2017). However, in old neutron stars reduction of glitching activities and dissipation of magnetic field gradually decreases \dot{E} and may reduce R_{TS} . Recent observation of thermal material at a relatively short distance of ~ 200 AU $\sim 3 \times 10^{15}$ cm around the isolated neutron star RXJ0806.4-4123 with an age of ~ 10 Myr (Posselt et al. 2018) is an example of such cases. On the other hand, during BNS formation and merger if neutron stars were initially at a distance $\gtrsim R_{TS}$ and if there were still a remnant of their wind nebula around them, its content as well as any other material would be disrupted. Moreover, during early stages of inspiral glitching activities and mass ejection might have been resumed due to perturbation of neutron stars crust and might have replenished the nebula. These processes can explain the putative additional surrounding material and its anisotropic distribution according to the model presented here.

To estimate column density of this material we can use distribution used in the model i.e. $N(r) = N(r_0)(r/r_0)^{-\kappa}$. For model C1 this estimation gives a column density of $\sim 4 \times 10^{14}$ cm $^{-2}$ for swept material from centre to the site of external shocks. It is much smaller than column density of C1, which has the smallest column density among components of the model. It is also smaller than swept material in the first $\sim 3 \times 10^5$ s after the onset of the external shocks, and therefore is completely negligible. See also Figs B1(d) and (e) for simulation of shocks on the ISM/circumburst material with the same density as C1 but at shorter distances from the

centre. On the other hand, if we consider much denser circumburst material at shorter distances, much higher X-ray flux generated by the shocks violates upper limits at $\sim T + 2$ d, see Fig. B1(f) for an example with $\dot{N} = 4 \text{ cm}^{-3}$, i.e. 2 orders of magnitude larger than in C1 in Table 1, in which the early X-ray flux is about 2 orders of magnitude larger than upper limits. In such a model the column density of material between sites of internal and external shocks would be $\sim 4 \times 10^{16} \text{ cm}^{-2}$. Using these simulations and estimations, we conclude that the column density of material inside $r_e \sim 10^{16}$ was $< \mathcal{O}(1) \times 10^{15} \text{ cm}^{-2}$ or equivalently its average density was $< 0.4 \text{ cm}^{-3}$.

In conclusion, diversity of short GRB afterglows reflect age, history, and environmental differences of progenitor neutron stars. In the case of GW/GRB 170817A we notice that \dot{N} is much smaller than typical values predicted for young neutron stars/pulsars (Slane 2017). This means that the progenitor stars were most probably old and had lost most of material they had ejected during their youth. This conclusion is consistent with analysis of the prompt gamma-ray of this transient (Ziaeeepour 2018). The relatively large distance of circumburst material may have several reasons, but with available information about progenitors it is not possible to pin down the dominant cause.

4 OUTLINE

In this work we used the same phenomenological formulation which had been used to model the prompt gamma-ray emission of GW/GRB 170817A to analyse its afterglows. We found a three-component model presenting a structured relativistic jet which its collision with circumburst material at a distance of ~ 1000 AU generated observed afterglows. It reproduces radio and X-ray light curves and photometric spectrum in these bands. Its optical emission is consistent with the dominance of the kilonova emission in this band up to $\gtrsim 200\text{--}300$ d after the merger event, where this range covers degeneracy of models studied here.

Additionally, this analysis helps understand physical conditions around the progenitor BNS before and after their merger. In particular, it shows that a small fraction of the prompt ultra-relativistic jet had survived internal shocks, and despite dissipation and lateral expansion it had preserved in some extent its internal coherence up to a distance of $\sim 10^{16}$ cm from central source, where it collided with surrounding material. Another result of the model studied here is that despite oblique view of the jet, our line of sight passed through an ultra-relativistic region. This conclusion is consistent with works in the literature which fit observations up to 200 d post merger and beyond. It seems that an ultra-relativistic component is indispensable for a proper fit of the whole data. Other components of the model, which their emissions are dominantly in low energies, are interpreted as approximately presenting side lobes/cocoon of a structured jet at the time of external shocks.

The line of sight angle is model dependent and correlated to the jet profile and its maximum – on-axis – Lorentz factor. In the models studied here it can be as small as $\sim 5^\circ$ for a maximum Lorentz factor of ~ 250 or as large as $\sim 18^\circ$ if on-axis Lorentz factor approached 1000. Considering observed orbital inclination of the BNS and superluminal motion of the radio counterpart, and marginalizing on the models and their parameters, the line of sight angle can be estimated as $5^\circ\text{--}18^\circ$.

We identified low density of circumburst material from merger, its low density and low density of the jet as factors leading to slow rise of afterglows. Relatively long distance of the circumburst materials from centre might have been in part the reason for extended expansion of the jet up to longer distances than in typical short

bursts and its dilation, which in addition to slow rise of afterglows, pushed the peak of emission to $\gtrsim 110$ d, rather than a couple of days seen in short GRBs with a X-ray plateau. Unfortunately, in absence of long duration follow up of short GRBs we are not able to access whether late shocks and brightening is an exception in this burst or a common behaviour of many short GRBs, i.e. those for which an early X-ray plateau is not observed.

ACKNOWLEDGEMENTS

The author thanks Hans Krimm for providing the unpublished upper limit of the Swift-BAT on the late gamma-ray emission from GW/GRB 170817, and Amy Lien and Scott Barthelmy from Swift Science Team for their help to acquire this data.

REFERENCES

- Alexander K. D. et al., 2017, *ApJ*, 848, L21
 Alexander K. D. et al., 2018, *ApJ*, 863, L18
 Beuermann K. et al., 1999, *A&A*, 352, L26
 Chatterjee S., Cordes J. M., 2004, *ApJ*, 600, L51
 Covino S. et al., 2017, *Nat. Astron.*, 1, 791
 Cowperthwaite P. S. et al., 2017, *ApJ*, 848, 17
 D’Avanzo P. et al., 2018, *A&A*, 613, L1
 D’Elia V. et al., 2011, *GCN Circ.* 11705
 Dingus B. L., 1995, *Space Sci.*, 231, 187
 Dionysopoulou K., Alic D., Rezzolla L., 2015, *Phys. Rev. D*, 92, 084064
 Dobie D. et al., 2018, *ApJ*, 858, L15
 Duffell P. C., MacFadyen A. I., 2013, *ApJ*, 775, 87
 Duffell P. C., Quataert E., MacFadyen A. I., 2015, *ApJ*, 813, 64
 Evans P. A. et al., 2017, *Science*, 358, 1565
 Fong W. F. et al., 2013, *ApJ*, 780, 118
 Fong W. F., Berger E., Margutti R., Zauderer B. A., 2015, *ApJ*, 815, 102
 Fong W. F. et al., 2017, *ApJ*, 848, L29
 Ghirlanda G. et al., 2019, *Science*, 363, 968
 Goldstein A., Veres P., Burns E., Briggs M. S., Hamburg R., Kocevski D., Wilson-Hodge C. A., Preece R. D., 2017, *ApJ*, 848, L14
 Gottlieb O., Nakar E., Piran T., Hotokezaka K., 2018, *MNRAS*, 479, 588
 Grano J., Piran T., 2012, *MNRAS*, 421, 570
 Haggard D., Nynka M., Ruan J. J., 2018, *GCN Circ.* 23137, Correction: *GCN Circ.*
 Hajela A., Alexander K. D., Eftekhari T., Margutti R., Fong W., Berger E., 2018, *GCN Circ.* 22692
 Hallinan G. et al., 2017, *Science*, 358, 1579
 Hotokezaka K., Kiuchi K., Shibata M., Nakar E., Piran T., 2018, *ApJ*, 867, 95
 Izzo L. et al., 2019, *Nature*, 565, 324
 Kann D. A., 2013, *EAS Publ. Ser.*, 61, 309
 Kasen D., Barnes J., 2019, *ApJ*, 876, 128
 Kasen D., Metzger B., Barnes J., Quataert E., Ramirez-Ruiz E., 2017, *Nature*, 551, 80
 Kasliwal M. M. et al., 2017, *Science*, 358, 1559
 Kiuchi K., Sekiguchi Y., Kyutoku K., Shibata M., Taniguchi K., Wada T., 2015, *Phys. Rev. D*, 92, 064034
 Komisarov S., Vlahakis N., Konigl A., Barkov M., 2009, *MNRAS*, 394, 1182
 Lamb G. P., Kobayashi S., 2017, *MNRAS*, 472, 4953
 Lamb G. P. et al., 2019, *ApJ*, 870, L15
 Lazzati D., Deich A., Morsony B. J., Workman J. C., 2017, *MNRAS*, 471, 1652
 Lazzati D., Perna R., Morsony B. J., López-Cámara D., Cantiello M., Ciolfi R., Giacomazzo B., Workman J. C., 2018, *Phys. Rev. Lett.*, 120, 241103
 LIGO Scientific Collaboration, 2017a, *ApJ*, 848, L12
 LIGO Scientific Collaboration, Virgo Collaboration, Fermi Gamma-Ray Burst Monitor Collaboration, INTEGRAL Collaboration, 2017b, *ApJ*, 848, L13
 Lind K. R., Blandford R. D., 1985, *ApJ*, 295, 358
 Lyman J. D. et al., 2017, *Nat. Astron.*, 2, 751

Mandel I., 2018, *ApJ.*, 853, L12
 Margutti R. et al., 2017, *ApJ*, 848, L20
 Margutti R. et al., 2018, *ApJ*, 856, L18
 Marshall F. E. et al., 2007, *GCN Circ.* 6728
 Metzger B. D., Thompson T. A., Quataert E., 2018, *ApJ.*, 856, 101
 Montanari E., Frontera F., Guidorzi C., Rapisarda M., 2005, *ApJ.*, 625, L17
 Mooley K. P. et al., 2018, *Nature*, 554, 207
 Mooley K. P. et al., 2018a, *Nature*, 561, 355
 Mooley K. P. et al., 2018b, *ApJ*, 868, L11
 Murguia-Berthier A. et al., 2017, *ApJ*, 848, L34
 Nakar E., Gottlieb O., Piran T., Kasliwal M. M., Hallinan G., 2018, *ApJ*, 867, 18
 Nicholl M. et al., 2017, *ApJ*, 848, 18
 Nishikawa K. I. et al., 2016, *ApJ.*, 820, 94
 Norris J. P., Gehrels N., Scargle J. D., 2010, *ApJ.*, 717, 411
 Nynka M., Ruan J. J., Haggard D., Evans P. A., 2018, *ApJ*, 862, L19
 Olivares F. et al., 2012, *A&A*, 539, A76
 Pian E. et al., 2017, *Nature*, 551, 67
 Piro L., Kollmeier J., 2018, *ApJ.*, 855, 103
 Posselt B., Pavlov G. G., Ertan Ü., Çalikın S., Luhman K. L., Williams C. C., 2018, *ApJ*, 865, 1
 Rossi E. M., Lazzati D., Salmonson J. D., Ghisellini G., 2004, *MNRAS*, 354, 86
 Rossi A. et al., 2018, *GCN Circ.* 22763
 Rybicki G. B., Lightman A. P., 2004, *Radiative Processes in Astrophysics.* Wiley-VCH verlag GmbH & Co.KGAA, Weinheim
 Sari R., Piran T., Narayan R., 1998, *ApJ.*, 497, 17
 Savchenko V. et al., 2017, *ApJ*, 848, L15
 Slane P., 2017, in Alsabti A. W., Murdin P., eds, *Handbook of Supernovae* 2159. Springer, Cham
 Smartt S. J. et al., 2017, *Nature*, 551, 75
 Soares-Santos M. et al., 2017, *ApJ*, 848, L16
 Spitkovsky A., 2008, *ApJ.*, 682, 5
 Takami K., Yamazaki R., Sakamoto T., Sato G., 2007, *ApJ.*, 663, 1118
 Troja E. et al., 2017, *Nature*, 551, 71
 Troja E., Piro L., Ryan G., 2018, *GCN Circ.* 22693
 Troja E. et al., 2018, *MNRAS*, 478, L18
 Troja E. et al., 2019, *MNRAS*, 489, 1919
 Tunnicliffe R. L. et al., 2014, *MNRAS*, 437, 1495
 Waxman E., Ofek E. O., Kushnir D., 2019, *ApJ.*, 878, 93
 Willingale R. et al., 2007, *ApJ.*, 662, 1093

Winkler C. et al., 2003, *A&A*, 411, L1.
 Wu Y., MacFadyen A., 2019, *ApJ.*, 869, 55
 Xie X., Zrake J., MacFadyen A., 2018, *ApJ.*, 863, 58
 Ziaeeepour H., 2009, *MNRAS*, 397, 361
 Ziaeeepour H., 2018, *MNRAS*, 478, 3233
 Ziaeeepour H., 2019, *Physics*, 1, 194
 Ziaeeepour H., Gardner B., 2011, *J. Cosmol. Astropart. Phys.*, 2011, 001
 Ziaeeepour H. et al., 2007, *GCN Rep.* 74.2

APPENDIX A: DEFINITION OF PARAMETERS AND EVOLUTION OF ACTIVE REGION

Note that in the formulation model in Ziaeeepour (2009) and Ziaeeepour & Gardner (2011) Γ is the Lorentz factor slow shell with respect to a far observer and γ'_0 indicates the relative Lorentz factor fast and slow shells. In external shocks on the ISM or circumburst material, their velocity is negligible and $\Gamma = 1$. For this reason, here we have replaced γ'_0 with Γ which is usually used in the literature and indicates the Lorentz factor of outflow at the beginning of external shocks.

As explained in Section 3.3.2 the evolution of $\Delta r'(r')$ cannot be determined from first principles. For this reason we consider the following phenomenological models:

$$\Delta r' = \Delta r'_0 \left(\frac{\gamma'_0 \beta'}{\beta'_0 \gamma'} \right)^\tau \Theta(r' - r'_0) \quad \text{dynamical model, Model = 0} \quad (\text{A1})$$

$$\Delta r' = \Delta r'_\infty \left[1 - \left(\frac{r'}{r'_0} \right)^{-\delta} \right] \Theta(r' - r'_0) \quad \text{Steady state model, Model = 1} \quad (\text{A2})$$

$$\Delta r' = \Delta r'_0 \left(\frac{r'}{r'_0} \right)^{-\delta} \Theta(r' - r'_0) \quad \text{Power-law model, Model = 2} \quad (\text{A3})$$

Table A1. Parameters of the phenomenological relativistic shock model.

Model (mod.)	Model for evolution of active region with distance from central engine.
r_0 (cm)	Initial distance of shock front from central engine.
Δr_0	Initial (or final, depending on the model) thickness of active region.
p	Slope of power-law spectrum for accelerated electrons; see equation (3.8) of Ziaeeepour & Gardner (2011).
p_1, p_2	Slopes of double power-law spectrum for accelerated electrons; see equation (3.14) of Ziaeeepour & Gardner (2011).
γ_{cut}	Cut-off Lorentz factor in power law with exponential cut-off spectrum for accelerated electrons; see equation (3.11) of Ziaeeepour & Gardner (2011).
Γ	Lorentz factor of jet with respect to far observer.
δ	Index in the model defined in equation (3.29) of Ziaeeepour & Gardner (2011).
Y_e	Electron yield defined as the ratio of electron (or proton) number density to baryon number density.
ϵ_e	Fraction of the kinetic energy of falling baryons of fast shell transferred to leptons in the slow shell (defined in the slow shell frame).
α_e	Power index of ϵ_e as a function of r .
ϵ_B	Fraction of baryons kinetic energy transferred to induced magnetic field in the active region.
α_B	Power index of ϵ_B as a function of r .
N'	Baryon number density of slow shell.
κ	Power-law index for N' dependence on r' .
n'_c	Column density of fast shell at r'_0 .

Notes. *The phenomenological model discussed in Ziaeeepour (2009) and its simulation (Ziaeeepour & Gardner 2011) depends only on the combination $Y_e \epsilon_e$. For this reason only the value of this combination is given for simulations.

*The model neglects variation of physical properties along the jet or active region. They only depend on the average distance from centre r , that is $r - r_0 \propto t - t_0$.

*Quantities with prime are defined with respect to rest frame of slow shell, and without prime with respect to central object, which is assumed to be at rest with respect to a far observer. Power indices do not follow this rule.

$$\Delta r' = \Delta r_\infty \left[1 - \exp\left(-\frac{\delta(r' - r'_0)}{r'_0}\right) \right] \Theta(r - r'_0)$$

Exponential model, Model = 3 (A4)

$$\Delta r' = \Delta r'_0 \exp\left(-\delta \frac{r'}{r'_0}\right) \Theta(r' - r'_0)$$

Exponential decay model, Model = 4 (A5)

The column called Model in Table A1 refers to these evolution models for $\Delta r'(r')$. The initial width $\Delta r'(r'_0)$ in Model = 1 & 3 is zero. Therefore, they are suitable for description of initial formation of an active region in internal or external shocks. Other models are suitable for describing more moderate growth or decline of the active region. In Table 1 the column *mod.* indicates which evolution rule is used in a simulation regime – as defined in the foot notes of this table – using model number given in A1–A5.

APPENDIX B: ALTERNATIVE MODELS FOR THE STRUCTURED JET OF GW/GRB 170817A

As mentioned in Section 2 the large number of parameters in the phenomenological formulation used here to model afterglows of GW/GRB 170817A does not allow to perform a systematic search in the parameters space to optimize selected models. Moreover, based on physical arguments there must be correlation between

parameters. Unfortunately in absence of a first-principle formalism they cannot be easily removed and induce degeneracies in the model.

To investigate how degeneracies affect the model of afterglows presented here and whether they can alter our conclusions, Figs B1, B2, and B3 show some variants of the model presented in Table 1. In most of these simulations only distance of shock from merger, Lorentz factor, column density of the jet, thickness of shocked (active) region, and density of ISM/circumburst material, are changed and other parameters are kept the same as ones shown in Table 1. In some models index of energy distribution of electrons p and fraction of energy transferred to electric field ϵ_e are also changed.

Although some of these models fit the data as good as the model of Table 1, they have some issues which we will discuss case by case. For instance, a variant of C1 with larger $\Delta r_0/r_0$ and smaller ISM/circumburst density presented in Fig. B1(b) is degenerate with C1 in Table 1, but future observations of X-ray afterglow can distinguish between them. A variant of C2 with larger $\Delta r_0/r_0$ and smaller ϵ_b shown in Fig. B2(d) has a slightly better fit to the data. But it is not exactly a replacement of C2 and can be considered as a finer division of the structured jet to components.

In the following subsections we summarize properties of variant models separately for each component.

B1 Variants of C1

Fig. B1 shows variants of component C1. In model (a) density of ISM/circumburst material is smaller and consequently its X-

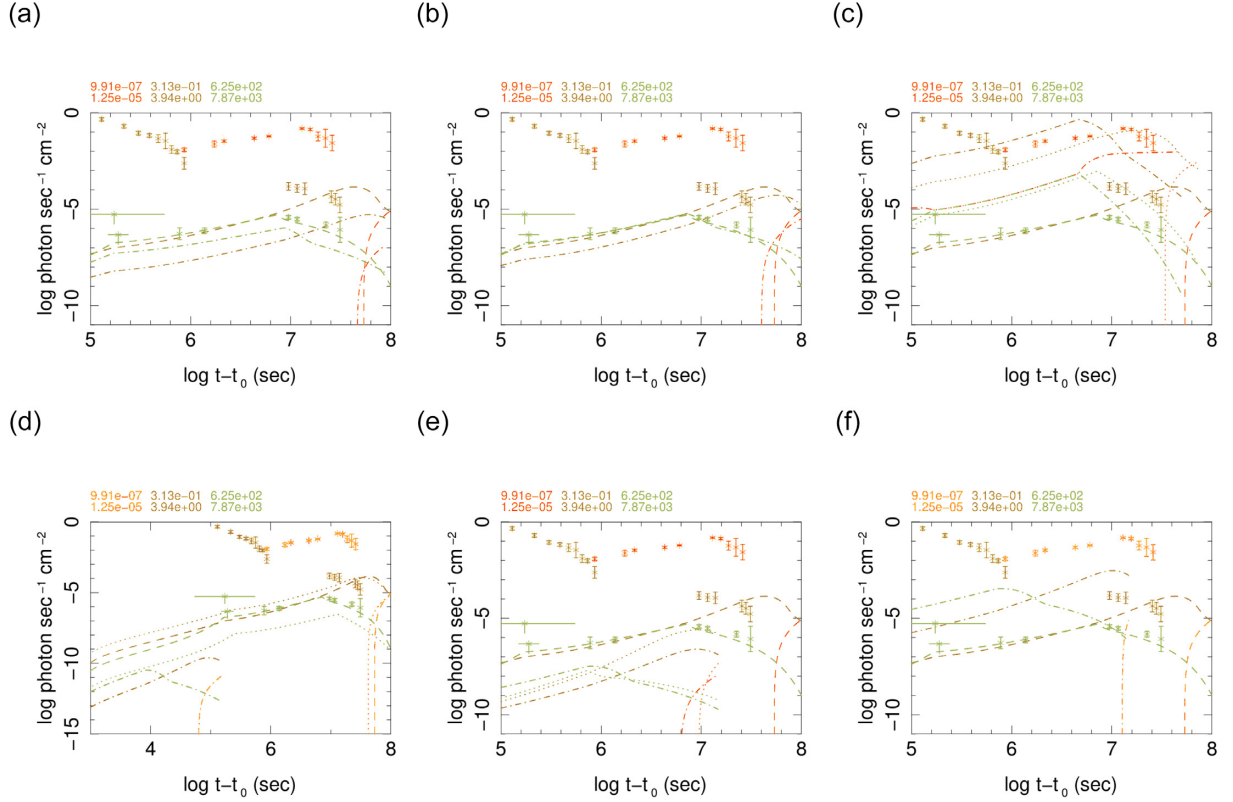


Figure B1. Models of component C1 with varied parameters: (a) $N' = 0.008 \text{ cm}^{-3}$ (dash-dot); (b) $\Delta r_0/r_0 = 10^{-6}$, $N' = 0.004 \text{ cm}^{-3}$ (dash-dot); (c) $\gamma'_0 = \Gamma = 8$; $\Delta r_0/r_0 = 5 \times 10^{-3}$, $p = 2.1$, $N' = 0.03 \text{ cm}^{-3}$, $n'_c = 5 \times 10^{23} \text{ cm}^{-2}$ (dash-dot), $\gamma'_0 = \Gamma = 80$; $\Delta r_0/r_0 = 3 \times 10^{-4}$, $p = 2.1$, $N' = 0.03 \text{ cm}^{-3}$, $n'_c = 5 \times 10^{22} \text{ cm}^{-2}$ (dotted); (d) $r_0 = 10^{13} \text{ cm}$, $\Delta r_0/r_0 = 10^{-4}$, $n'_c = 10^{23} \text{ cm}^{-2}$ (dash-dot); $r_0 = 1.5 \times 10^{16} \text{ cm}$, $\Delta r_0/r_0 = 10^{-6}$, $p = 2.1$, $\epsilon_e = 0.02$, $N' = 0.008 \text{ cm}^{-3}$, $n'_c = 5 \times 10^{23} \text{ cm}^{-2}$ (dotted); (e) $r_0 = 10^{15} \text{ cm}$, $n'_c = 5 \times 10^{23} \text{ cm}^{-2}$ (dash-dot); $r_0 = 10^{15} \text{ cm}$, $n'_c = 5 \times 10^{24} \text{ cm}^{-2}$, $\kappa = 0$, i.e. a uniform ISM/circum-burst density (dotted) (f) $r_0 = 10^{15} \text{ cm}$, $n'_c = 5 \times 10^{24} \text{ cm}^{-2}$, $N' = 4 \text{ cm}^{-3}$ (dash-dot). Other parameters of these models are the same as model C1 in Table 1. In all plots dash line corresponds to component C1 in this table. Note that simulated optical light curves have a broader width than in Fig. 1.

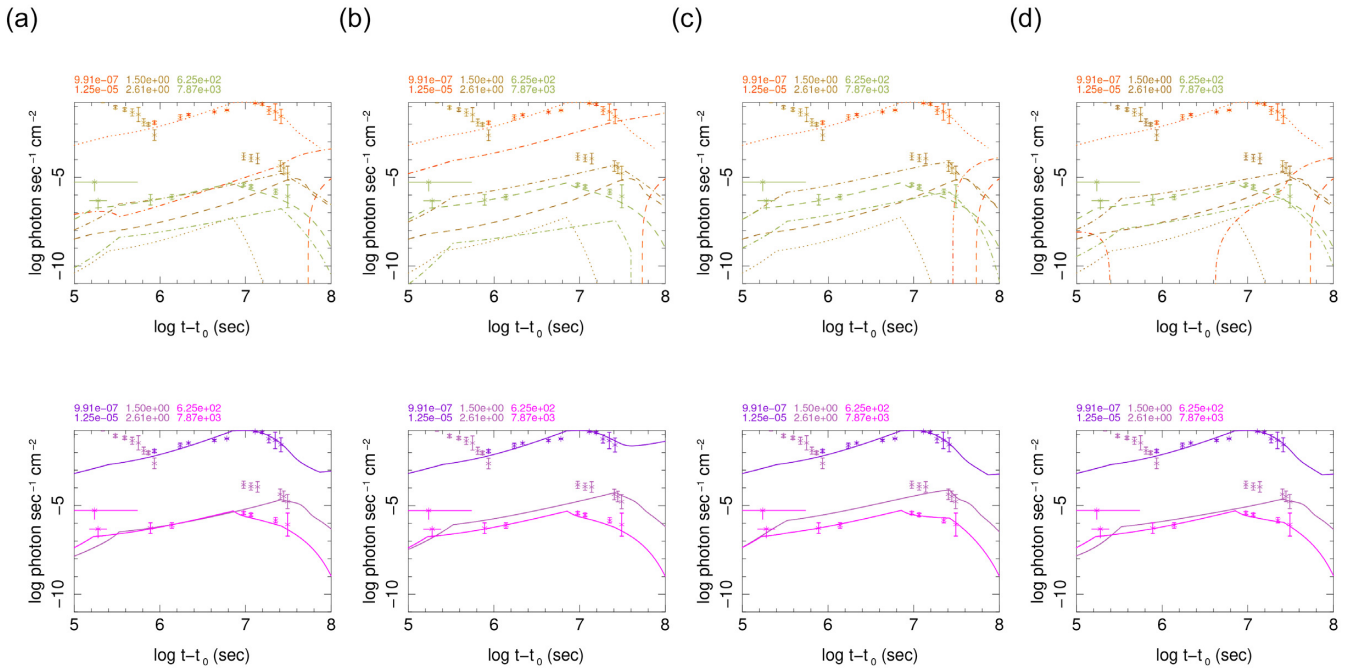


Figure B2. Light curves of three-component model with variant component C2. Upper row: Light curves of components; Lower row: Sum of light curves of three components. Variant of C2 have following parameters different from C2 in Table 1: (a) $\Delta r_0/r_0 = 10^{-3}$; (b) $\Delta r_0/r_0 = 5 \times 10^{-4}$, $\epsilon_e = 0.03$, $N' = 0.02 \text{ cm}^{-3}$; (c) $\gamma'_0 = \Gamma = 30$, $\Delta r_0/r_0 = 10^{-6}$, $n'_e = 10^{22} \text{ cm}^{-2}$; (d) $\gamma'_0 = \Gamma = 30$, $\Delta r_0/r_0 = 10^{-5}$, $n'_e = 10^{22} \text{ cm}^{-2}$, $N' = 0.008 \text{ cm}^{-3}$. C1 and C3 correspond to models shown in Table 1. Definition of light curves is the same as in Fig. 1.

ray emission is not sufficient. Model (b) has larger $\Delta r_0/r_0$ but smaller ISM/circumburst density, which falls in the lower half of the range of ISM/circumburst material density estimated for other short GRBs (Fong et al. 2015). This model is an example of a model degenerate with C1 in Table 1. However, it has flatter X-ray light curve at later times, i.e. after $T + 4 \times 10^7 \text{ s} \sim T + 470 \text{ d}$. Thus, future observations may distinguish between this model and C1 in Table 1. None of models in Figs B1(a) or (b) can explain the radio afterglow. Fig. B1(c) includes two models with smaller Lorentz factors, larger $\Delta r_0/r_0$, and larger ISM/circumburst and/or jet column densities. Both models have inconsistent X-ray and optical light curves and insufficient radio emission. We also notice that although r_0 in these models is the same as C1 in Table 1, the time of peaks in the same bands are not the same in the three models.

Fig. B1(d) presents two models, one with a shorter initial radius r_0 for external shocks and the other with a longer distance. The most important difference of these models with C1 in Table 1 is the time of peak emission. Although the amplitude of X-ray light curves of these models are low, it can be adjusted by increasing $\Delta r_0/r_0$ and/or column density. Therefore, the essential problem of these models is the position of light curves peaks. Model (e) has r_0 less than C1 but larger than the first model in Fig. B1(d) and a jet column density one order of magnitude larger than C1. Similar to models in Fig. B1(d) the time of peak emission and its amplitude are inconsistent with data. Finally, model (f) has similar distance as the model in Fig. B1(e) but higher jet column density and ISM/circumburst material density. It is too bright in X-ray and optical and peaks are too early.

B2 Variants of C2

As mentioned in Section 2, optical and IR emissions are dominantly from kilonova and only during the latest observations at

$>T + 200 \text{ d}$ contribution of the GRB might have become significant. For this reason optical data should be used as an upper limit for GRB contribution. It is also more difficult to select the best model for C2 and quantify characteristics of the component/section of the jet which emitted dominantly in optical bands.

Fig. B2 shows light curves of components and their sum for four variant models to C2 in Table 1. Model (a) has a smaller $\Delta r_0/r_0$ and predicts a lower contribution from GRB in the optical/IR emission than C2. Model (b) has a larger $\Delta r_0/r_0$ than C2 but smaller ISM/circumburst density and fraction of kinetic energy transferred to accelerated electrons. This model fits the last three optical/IR observations and has a slightly better fit $-\chi^2 \approx 1.57$ for C2 against $\chi^2 \approx 0.05$ for this model (only the last three data points are considered). However, the model in Fig. B2(b) may be also interpreted as slightly overestimating optical emission at the epoch of latest three observations.

Models (c) and (d) are simulated with $\Gamma = 30$, i.e. similar to the second prompt gamma-ray peak at the end of internal shocks (Ziaeeepour 2018a). The purpose for this choice is to see whether C2 can be a remnant of shells or sector of jet creating the second prompt peak. Interestingly, they fit X-ray light curve slightly better than model C1 in Table 1 because they have a significant X-ray emission at late times. But (c) slightly overestimates optical emission. This inconsistency can be resolved by e.g. slightly reducing the width of active region or column density. However, such adjustments decrease its X-ray contribution too and neutralizes advantage of this model with respect to the model of Table 1. Model (d) has both X-ray and optical well consistent with the data. However, the density of ISM/circumburst material in this model is five folds less than in C1 component. Giving the fact that radiation from models (c) and (d) should come from an azimuthal angle $\lesssim 2^\circ$ further from C1, such a large variation of ISM/circumburst density seems unrealistic. By contrast, if in place of C1 we use its variant in Fig. B1(b), which has

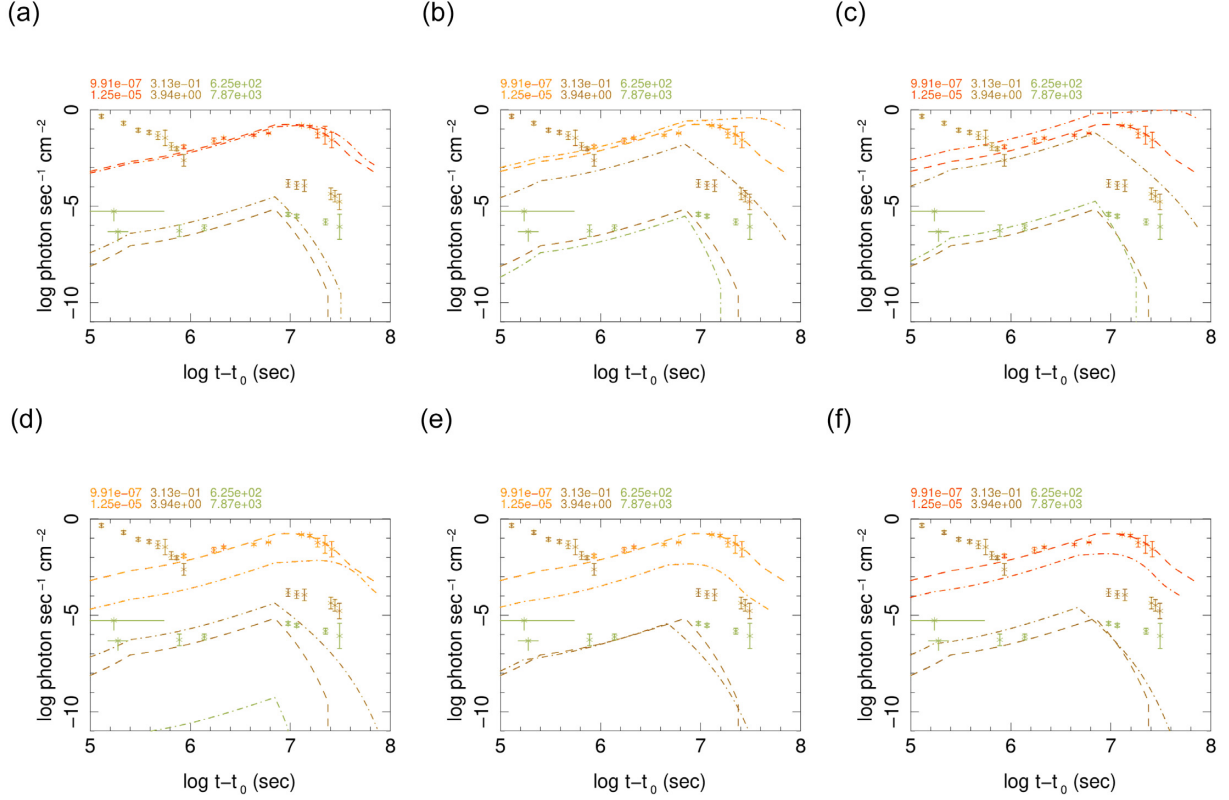


Figure B3. Models of component C3 with varied parameters: (a) $\gamma'_0 = \Gamma = 4$, $r_0 = 10^{16}$ cm, $\Delta r_0/r_0 = 10^{-3}$, $N' = 0.001$ cm $^{-3}$, $n'_c = 10^{25}$ cm $^{-2}$ (dash-dot); (b) $\gamma'_0 = \Gamma = 4$, $r_0 = 10^{16}$ cm, $\Delta r_0/r_0 = 10^{-3}$, $n'_c = 10^{25}$ cm $^{-2}$ (dash-dot); (c) $\gamma'_0 = \Gamma = 4$, $r_0 = 10^{16}$ cm, $\Delta r_0/r_0 = 10^{-3}$, $N' = 0.04$ cm $^{-3}$, $n'_c = 10^{25}$ cm $^{-2}$ (dash-dot); (d) $\gamma'_0 = \Gamma = 1.6$ cm $^{-2}$, $r_0 = 10^{16}$ cm (dash-dot); (e) $\gamma'_0 = \Gamma = 1.6$, $r_0 = 10^{16}$ cm, $\Delta r_0/r_0 = 10^{-3}$ (dash-dot); (f) $\gamma'_0 = \Gamma = 1.6$, $r_0 = 10^{16}$ cm, $\Delta r_0/r_0 = 10^{-3}$, $n'_c = 10^{25}$ cm $^{-2}$ (dash-dot). Other parameters of these models are the same as model C3 in Table 1. In all plots dash lines corresponds to component C3 in Table 1. Note that optical band in these plots have a broader width than in Fig. 1.

much smaller ISM/circumburst density closer to that of model (d) here, then together with (d) for C2 they make an overall consistent model. In any case, column density of (c) and (d) models is much smaller than other components. In a picture in which the three-component model crudely presents profile of the jet, a component with a tiny column density can be included to more prominent ones and neglected. As mentioned in the footnote 5, a better model of the jet should include continuous variation of column density and Lorentz factor with azimuthal angle.

B3 Variants of C3

Fig. B3 shows variant models for component C3. Models B3-a, -b, -c have a Lorentz factor of 4, i.e. similar to estimation of Mooley et al. (2018a) from observation of superluminal movement of radio counterpart. Model (a) has a shorter initial distance r_0 from centre, thinner active region, and lower ISM/circumburst material density, and denser jet. Radio light curve of this model is consistent with data up to $\sim T + 2 \times 10^7$ s ~ 230 d. This date corresponds to the second epoch of observations reported in Mooley et al. (2018a), which was used to measure apparent superluminal displacement of the source. However, C3 model in Table 1 fits later observations better. Nonetheless, considering uncertainties of the data, this model a priori remains an acceptable alternative. On the other hand, a column density of $\sim 10^{25}$ cm $^{-2}$ in (a) seems too large to be realistic. Indeed this is equal to the column density of the ultra-

relativistic component at much closer distances to the merger and before prompt internal shocks. Energy dissipation in the outflow during its propagation from site of internal shocks up to location of external shocks should have reduced column density unless it had kept its coherence and collimation, and thereby its kinetic energy and Lorentz factor. But reduction of Γ from 130 to just 4 is inconsistent with these assumptions. Another way to reconcile model (a) with the overall picture is to assume that it is dominated by less accelerated, initially unshocked material ejected by the merger at azimuthal angles between ultra-relativistic component and slow kilonova disc/torus. A component with these properties may be present in some GRMHD simulations, for instance those by Dionysopoulou, Alic & Rezzolla (2015) and Kiuchi et al. (2015). In any case, replacing C3 in Table 1 with (a) does not significantly modify conclusions of Section 3.

Models (b) and (c) have larger ISM/circumburst density and overproduce both optical and radio emissions. Models (d), (e), and (f) have a Lorentz factor slightly larger than C3 in Table 1 and r_0 shorter by 50 per cent. None of them produces enough radio emission even with a column density n'_c as large as 10^{25} cm $^{-2}$. These models show the interplay between Lorentz factor, densities, and thickness of active synchrotron emitting region.

This paper has been typeset from a $\text{\TeX}/\text{\LaTeX}$ file prepared by the author.